Directional HF Antennas Exploiting Electrically Small Radiating Elements

by

Rubén F. M. Delgado Castillo

A dissertation submitted in partial fulfillment of the requirements for the degree of

Doctor of Philosophy
(Electrical Engineering)

at the

University of Wisconsin-Madison

2022

Date of final oral examination: 10/04/2022

The dissertation is approved by the following members of the Final Oral Committee:

Nader Behdad, Professor, Electrical and Computer Engineering
John H. Booske, Professor, Electrical and Computer Engineering
Zongfu Yu, Professor, Electrical and Computer Engineering
Alan McMillan, Professor, Radiology and Medical Physics

Contents

1	Intr	roduct	ion	1	
	1.1	Motivation			
	1.2	Litera	ture Review on Electrically-Small, Directional HF Antennas	4	
		1.2.1	Platform-Based Antennas	4	
		1.2.2	Near-Vertical Incidence Skywave Communications	5	
		1.2.3	Multiple-Input Multiple-Output Systems	6	
		1.2.4	Distributed Transmit Beamforming	6	
	1.3	Propo	sed Solutions	7	
		1.3.1	Platform-Based, Electrically-Small HF Antenna With Switchable Di-		
			rectional Radiation Patterns	7	
		1.3.2	Capacity Analysis of Ship-to-Shore HF MIMO Systems Employing a		
			Single-Hop Ionospheric Channel	8	
		1.3.3	Future Work	(
2	Pla	tform-	Based, Electrically-Small HF Antenna With Switchable Direc-		
	tion	nal Rac	diation Patterns	10	
	2.1	Introd	luction	11	
	2.2	Anten	na Design	13	
		2.2.1	The Characteristic Mode Analysis of the Platform	14	
		2.2.2	Designing Coupling Structures	16	
		2.2.3	Cardioid-Shaped Pattern Generation Using Excited Platform Modes .	20	
		2.2.4	Feed Network Design	22	
	2.3	Exper	imental Results	24	
		2.3.1	Design of the Scaled-Model Antenna Prototype	24	
		2.3.2	Fabrication Process	26	

		2.3.3	Measurement Results	28
	2.4	Concl	asion	32
3	Cap	acity	Analysis of Ship-to-Shore HF MIMO Systems Employing a	
	Sing	gle-Ho	p Ionospheric Channel	3 4
	3.1	Introd	uction	35
	3.2	Single	-Hop, Ionospheric MIMO Channel Modeling	36
		3.2.1	Propagation Modeling	37
		3.2.2	Ionospheric Mode of Propagation	40
		3.2.3	Channel Capacity	41
	3.3	Anten	na Configuration	41
		3.3.1	Design Procedure	42
		3.3.2	Design Coupling Structures	44
		3.3.3	Feed Network Design	47
	3.4	Exper	imental Results	50
		3.4.1	Design of the Scaled-Model Antenna Prototype	50
		3.4.2	Fabrication Process	51
		3.4.3	Measurement Results	53
	3.5	Concl	asion	57
4	Fut	ure W	ork	59
	4.1	Exper	imental Demonstration of a Primary-Secondary Synchronization for Dis-	
		tribut	ed Transmit Beamforming Antenna Array	60
		4.1.1	Node Configuration for Experimental Demonstration	60
		4.1.2	Experimental Architecture on Distributed Transmit Beamforming	61
		4.1.3	Time-Slotted Synchronization Using GNURadio	62
$\mathbf{A}_{\mathbf{J}}$	ppen	dix		7 5

		iii
A	Supplementary Material	76
В	Ionosphere Modeling	78
С	Channel Capacity Study	80

List of Figures

2.1	Generation of a cardioid-shaped radiation pattern. (a) An omni-directional	
	radiation pattern. (b) A figure-eight-shaped radiation pattern. (c) A cardioid-	
	shaped radiation pattern generated by combining the omni-directional pattern	
	with the figure-eight-shaped pattern	13
2.2	Topology and dimensions of the platform used for the design presented in this	
	work	14
2.3	Simulated modal significance values of the first three modes of the AAV plat-	
	form shown in Fig. 2.2 when the platform is mounted on an infinite PEC	
	ground plane	15
2.4	Simulated normalized radiation patterns and surface current distributions of	
	the first three characteristic modes of the platform on an infinite PEC ground	
	plane at 12.5 MHz. (a) Mode 1, (b) Mode 2, (c) Mode 3	16
2.5	Topology of the coupling elements used to excite different modes of the plat-	
	form and the normalized radiation patterns that they generate. The platform	
	is mounted over an infinite PEC ground plane. (a) Two L-shaped monopoles	
	fed with the same excitation coefficient are used to excite Mode 1. (b) One	
	half-loop antenna, placed on the top surface of the platform is used to excite	
	Mode 2. (c) One half-loop antenna, placed on top rear edge of the platform is	
	used to excite Mode 3. All the coupling elements are designed with a copper	
	tube with a diameter of 71.8 mm	18
2.6	Final topology of the platform and the coupling elements mounted on it	2
2.7	Normalized cardioid-shaped radiation patterns, at 12.5 MHz, generated by	
	the platform-based antenna system shown in Fig. 2.6	21
2.8	Topology of the passive feeding and matching networks used in conjunction	
	with the coupling elements shown in Fig. 2.6	22

2.9	(a) A simplified scaled model of the platform on top of a circular-shaped	
	aluminum ground plane with radius of 0.41 m. (b) Simulated normalized	
	cardioid-shaped radiation patterns generated by this scaled-model prototype	
	in the azimuth plane at 437 MHz	25
2.10	Photographs of a 1:35 scaled-model fabricated prototype and its feed network.	
	Coaxial connectors are placed beneath the platform and connected to the feed	
	network inside the hollow 3-D platform. (a) 3-D printed platform with interior	
	cavities used to accommodate Mode 1 and 2 feed networks. (b) Photograph of	
	the rear section of the 3-D printed platform showing the cavity used to accom-	
	modate the Mode 3 feed network. (c)-(f) Layout and photographs of the feed	
	network designed to excite the different coupling elements. (g) Photographs	
	of the assembled scaled-model prototype	26
2.11	Measured S-parameters of the fabricated scaled-model prototype in the vicin-	
	ity of 630 MHz (corresponding to 18 MHz for the full-scale prototype)	30
2.12	Measured normalized, cardioid-shaped radiation patterns of the scaled-model	
	prototype shown in Figs. 2.9 and 2.10. (a) 437 MHz (12.5 MHz). (b) 630 $$	
	MHz (18 MHz). (c) 735 MHz (21 MHz)	30
3.1	Schematic illustrating a single-hop, ship-to-shore ionospheric channel with	
	multiple inputs and multiple outputs	37
3.2	Topology and dimensions of the platform used for the design presented in this	
	work	41
3.3	Simulated normalized radiation patterns and surface current distributions of	
	the first three characteristic modes of the platform on an infinite PEC ground	
	plane at 2 MHz. (a) Mode 1, (b) Mode 2, (c) Mode 3	42
3.4	NVIS MIMO channel capacity at 2 MHz using platform's CMs for a 2 \times 2	
	MIMO channel. (a) Modes 1 & 2, (b) Modes 1 & 3, (c) Mode 2 & 3	43

3.5	Topology of the resonators used to excite orthogonal characteristic modes of	
	the platform and the normalized radiation patterns with their corresponding	
	component. The platform is mounted over an infinite PEC ground plane. (a)	
	Platform structure with each resonator dimensions. (b) Normalized radiation	
	patterns of the resonator 1 on the NVIS frequencies. (c) Normalized radiation	
	patterns of the resonator 2 on the NVIS frequencies	46
3.6	Topology of the passive feeding and matching networks used in conjunction	
	with the coupling elements shown in 3.5	47
3.7	A simplified scaled model of the platform on top of a circular-shaped aluminum	
	ground plane with radius of 0.41 m. The radiation patterns is given to 2 MHz $$	
	since the ground is smaller than $\lambda/2$ for each sides	49
3.8	Photographs of a 1:310 scaled-model fabricated prototype and its feed net-	
	work. Coaxial connectors are placed beneath the platform and connected to	
	the feed network PCBs inside the hallow 3-D platform. (a)–(b) Layout and	
	photograph of the feed network designed to excite the resonators. (c) 3-D	
	printed platform design with interior cavities used to accommodate the res-	
	onators feed networks. Also, design includes a hold mechanics since platform	
	was fabricated in two parts. (d) 3-D printed platform assemble and covered	
	its surfaces with copper tape. (e) Scaled-model completely assemble over a	
	aluminum ground and placed on the anechoic chamber for radiation measure-	
	ments	52
3.9	${\it Measured S-parameters of the scaled-model of the platform-based NVIS\ MIMO}$	
	Channel capacity. Resonators Match to (a) 620 MHz (2 MHz), (b) 1860 MHz	
	(6 MHz), and (c) 3100 MHz (10 MHz)	54
3.10	Simulated and measured realized gain radiation patterns of the fabricated	
	prototype model at 620, 1860, and 3100 MHz	55

3.11	NVIS MIMO channel capacity using the two platform resonators with orthog-	
	onal dipoles above dry earth at shore. (a) 620 MHz, (b) 1860 MHz, and (c)	
	$3100~\mathrm{MHz}$ (corresponding to 2, 6, and 10 MHz for the full-scaled model)	56
4.1	HackRF One from Great Scott Gadget. Figure available from [79]	61
4.2	Disitributed transmit beamforming concentrating the beam direction toward	
	a desired target without any feedback from the target	62
4.3	GNU Radio software (a) receiver node schematic, (b) transmitting node schematic	
	This schematic used the local oscillator of the HackRF One	63
A.1	Detailed layout of the printed circuit boards that include the impedance	
	matching network and the baluns used to feed the antennas on the scaled-	
	model prototype. The top layout includes the feeding and matching network	
	for the coupling elements used to excite Mode 1 and 2 of the platform. The	
	bottom layout includes the feeding and matching network of the coupling el-	
	ement used to excite Mode 3. Table A.1 shows the corresponding values for	
	the variables.	76

A.2	Topology of one potential active feed network that can be used in the trans-	
	mit mode in conjunction with the proposed antennas to generate the desired	
	cardioid-shaped radiation patterns. Since the complex excitation coefficient	
	with which the different coupling elements must be excited will change as	
	a function of frequency and as a function of operational environment (e.g.,	
	changing different ground types, etc.), using an active feed network is ex-	
	pected to be more efficient. The circuit shown here depicts an active circuit	
	in the transmit mode. A similar circuit can be obtained for the receive mode if	
	the power amplifiers are replaced with low-noise amplifiers. A version of this	
	circuit that can be used for both transmit and receive applications requires	
	using transmit/receive switches to select between the low-noise amplifier in	
	the receive and the power amplifier in the transmit modes	77
B.1	Basic flowchart of the in-house algorithm used to calculate the NVIS MIMO	
	channel capacity for $M \times N$, but reduced the matrix based on needs	78
B.2	Tap-gain function represented as a power spectrum of a Gaussian scatter func-	
	tion. Each magneto-ionic component is represented by separated Gaussian	
	scatter functions. (a) Gaussian scatter power spectra. (b) Limited Gaussian	
	scatter power spectra.	79
C.1	NVIS MIMO channel capacity of the full size simulated platform with realistic	
	material details excited using the proposed resonators over the platform with	
	the orthogonal dipoles at shore. The channel capacity of the full size 2×2 at	
	(a) 2 MHz, (b) 6 MHz, and (c) 10 MHz	81

C.2	NVIS MIMO channel capacity of the simulated scaled-model platform with	
	all the realistic details before fabrication (i.e., copper tape, cardboard ground	
	cover with aluminum table, copper resonators, PCB, and lumped-elements).	
	The 2×2 channel capacity of the simulated scaled-model at (a) 620 MHz, (b)	
	$1860~\mathrm{MHz},~\mathrm{and}$ (c) $3100~\mathrm{MHz}$ (representing 2 MHz, 6 MHz, and 10 MHz,	
	respectively)	81
С.3	NVIS MIMO channel capacity of the measured scaled-model platform with	
	all the fabricated details of the proposed resonators over the platform. The	
	$2{\times}2$ channel capacity of the scaled-model at at (a) 2 MHz, (b) 6 MHz, and	
	(c) 10 MHz (representing 2 MHz, 6 MHz, and 10 MHz, respectively)	82

List of Tables

2.1	SIMULATED LOSS OF EACH SOURCE AND TOTAL EFFICIENCY OF THE EX-	
	CITED MODES FOR THE FULL-SCALE PLATFORM AT 12.5, 18, AND 21 MHz.	24
2.2	Component values of the matching networks of the simulated	
	AND FABRICATED SCALED MODEL AT 437, 630, AND 735 MHz	28
2.3	Measured S-parameters of the fabricated scaled-model proto-	
	TYPE IN THE VICINITY OF 437, 630, 735 MHz	29
2.4	EXCITATION COEFFICIENTS OF PORTS FOR GENERATING CARDIOID-SHAPED	
	RADIATION PATTERNS IN THE AZIMUTH PLANE. THE ORIENTATIONS ARE	
	BASED ON THE PLATFORM SHOWN IN FIG. 2.12	31
2.5	Measured realized gain of the Cardioid-Shaped radiation pat-	
	TERNS FOR THE SCALED-MODEL PROTOTYPE SHOWN IN FIGS. 2.9 AND	
	2.10	32
2.6	SIMULATED AND MEASURED TOTAL EFFICIENCIES OF THE COUPLING ELE-	
	MENTS USED TO EXCITE DIFFERENT MODES	32
3.1	SIMULATED LOSS OF EACH SOURCE AND TOTAL EFFICIENCY OF THE EX-	
	CITED MODES FOR THE FULL-SCALE PLATFORM AT $2,\ 6,\ \mathrm{AND}\ 10\ \mathrm{MHz}.$.	49
3.2	Lumped element Component values of the matching networks	
	OF THE SIMULATED AND FABRICATED SCALED MODEL AT 620, 1860, AND	
	3100 MHz	53
3.3	SIMULATED AND MEASURED TOTAL EFFICIENCIES OF THE COUPLING ELE-	
	MENTS USED TO EXCITE DIFFERENT MODES	56
A.1	Physical dimensions of the fabricated feed networks whose lay-	
	OUTS ARE SHOWN IN FIG. A.1.	77

Chapter 1

Introduction

1.1 Motivation

Directional antennas have the capability of focusing energy toward desired directions while decreasing energy on unwanted directions. Many applications require directional antennas implementations in the high-frequency (HF, 3–30 MHz) band. However, most conventional antennas are impractical because the large electromagnetic wavelengths in the HF band result in physically large structures [1]–[4]. Their wavelengths, at HF band, range from 100 m at 3 MHz to 10 m at 30 MHz. Hence, directional antennas require large physical area for placement. Definitely, for military systems directional antennas operating in the HF band are require, mostly, on moving platforms applications such like long-range communication, electronic warfare (EW), direction finding, and jamming.

In many instances, HF antennas for military in field missions are implemented on moving military platforms [5]–[8]. After all, platforms such as tanks, battleships, and airplanes have space constraints to accommodate such directional antennas. Therefore, antennas in the HF band on military platforms have significant linear size reductions. This physical limitation on electrically-small antenna (ESA) is commonly known as the Chu limit [9]. Numerous studies have examined the fundamental limitations of ESAs [9]–[11]. It is well-known that the physical size reduction of a regular antenna will result in a narrow bandwidth and low radiation efficiency. Additionally, ESAs would require impedance feed networks to reduce its large reactance and match its impedance to the port impedance. Many researchers have addressed these challenges by taking advantage of metallic platforms surrounding the antenna [12]–[17]. Taking this into account, most of the military platforms are made of metals, they exploited the platforms as the main radiator exciting it with coupling elements. Furthermore, the theory of characteristic modes can be utilized to find the locations for effective excitation of a platform with ESAs.

In addition to the implementation of ESAs near large metalic platforms to overcome their fundamental limitations, a technique based on multiple-input multiple-outputs (MIMO)

structures can be exploited to enhance the wireless data rates [18]. MIMO systems transmit different signals from each transmitter in order for the targe to receive a superposition of the signals [19]–[20]. However, the main challenge of the MIMO antenna designs is to provide high isolation between transmission and reception elements. In theory, the larger the spacing between elements, the higher the isolation. Although many other techniques have been studied, the high isolation between orthogonal polarized radiation patterns will provide better connection between reception and transmission [21]–[23]. Orthogonal polarizations for a metallic platform are usually obtained when the platform is electrically smaller than the electromagnetic wavelength. The characteristic mode theory is dependent on the platform's electrical size and shape. We can excite orthogonal characteristic modes and separate the antennas on a physically-large platform in the lower end of the HF band.

Other researcher improved HF antennas electrical limitations by exciting multiple radiator platforms instead of placing all the antennas over a single platform. Since in the HF band, the large electromagnetic wavelength would require huge spacing between radiators, researchers have been study isolated radio collaborations [24]–[26]. The radio collaborations, also known as radio distribution, has the same fundamental as array elements, but instead of exciting them with a single feed, it will require multiple antenna radios [24]. However, most recent studies are concentrated on commercial communication links between station towers to increase mobile long-range communications [27]–[29]. Nonetheless, implementing multiple synchronized radios with isolated radios can improve the overall efficiency toward desired target for military purposes. In theory, attaining distributed transmitted beamforming for EW application would require complete feedback independency from the target.

Due to various challenges associated with realizing electrically-small, efficient, and distributed transmit beamforming in the HF band, much research has to be conducted to address these challenges. These areas of research are outlined in the next section.

1.2 Literature Review on Electrically-Small, Directional HF Antennas

1.2.1 Platform-Based Antennas

In order to address the fundamental challenges associated with platform-based antennas, recent research has focused on the theory of characteristic modes (CMs). This concept was first introduced by Garbacz (1960s) [30]–[31] and later refined by Harrington and Mautz (1970s) [32]–[33]. The CMs of a platform and their associated current distributions can be obtained numerically for conducting bodies. The modal current distribution of a platform strictly depends on the shape and size of an object. Theses modes are considered to be significant if its modal significance value is larger than 0.7 at the operating frequency. It should be noted that a modal significant value of 1 indicates a resonant mode [8], [34].

In the past, this technique has been employed for mobile handset antenna designs with rectangular geometry representing cellphones [35]–[37]. The authors study the surface current and radiation patterns of the CM analysis and determine the right placement for coupling elements to conveniently enhance the antenna performances. Consequently, they selected effective coupling elements types to excite the platform CMs, while maintaining the platform profile of a cellphone. However, selecting a CM to excite depends on the application one is aiming for. For example, one can be interested in a specific radiation pattern for ground to ground or ground to air communications.

A variety of approaches have been used to address the problems associated with coupling elements. Many researchers have applied the theory of CMs to platform-based antennas that are electrically smaller than the wavelength [38]–[40]. In [12]–[16], in the HF band, the CMs of a platform are excited using coupling elements for military platforms. It should be noted that mounting ESAs on platforms larger than the antenna helps increase the effective maximum linear dimension resulting in bandwidth enhancement [12]–[13]. Therefore, the HF

band antennas over large metallic platforms are capable of enhancing the ESA limitations. The CM theory has also been used to manipulate the shape of the far-field radiation patterns by exciting multiple platform modes [13]. Furthermore, directional radiation patterns with pure CMs of a mid-size airplane were implemented to perform direction finding in the HF band [16].

1.2.2 Near-Vertical Incidence Skywave Communications

The lower end of the HF band (2–10 MHz) is highly useful for beyond line-of-sight (BLOS) communications. In the near-vertical incidence (NVIS) mode of communication at the HF band, the signal between the transmitter and receiver is bounced once from the ionosphere (i.e., a single-hop path) [41]–[43]. To effectively communicate at the HF band, several challenges must first be addressed [17]. First, due to the large wavelengths, physically large antennas are required. Moreover, the narrow coherence bandwidth of HF channels limits the amount of information transmitted over a single channel. In [44], study the interactions of a wave with the ionosphere layers. Layers like the D and E provide most of the absorption for NVIS communications. However, propagations in the HF band interact with the F-layer descomposing the wave in two orthogonal propagating modes called the ordinary (O) and the extraordinary (X) and bounce back to the ground. Many researchers has successfully estimated the ionosphere absorption and losses using integrals models for the D- and E-layers [45]–[46].

The ionosphere is a very complex which many researchers have try to predict the maximum frequency of operation, time, bandwidth, and even the concentration of plasmas for better models [47]–[48]. However, since the ionosphere is non stationary, researchers have tried simplifying the problem using simpler model. Most of those models limited the frequency band, the time of operations, and geolocation [48]. After limiting the propagating wave, the ionosphere model can be represented as a tap-gain model well known as Watterson model represented by a fading Gaussian scatter channel model. The model can be

implemented for multipath fading wave, but for our case we are interested in a single-hop individual split modes.

1.2.3 Multiple-Input Multiple-Output Systems

Multiple-input multiple-output (MIMO) wireless communications can be characterized by many different properties such as environment, wireless standard, carrier frequency, bandwidth, polarization, and others [19]. MIMO systems are highly identified by distributed beamforming solutions, such as synchronization, multiple distributed antenna elements, and channel estimation. One of the techniques implemented for recent mobile communication technology is the well-known frequency-division multiplexing [49]. This technology distributes the transmitted message over all the transmitting antennas. On the other hand, most military platforms have space constraints that makes it difficult to employ particular MIMO structure at HF band. However, designing antennas over a moving metallic platform with limited space improved their electrical parameters taking the platform CMs as part of the antenna design [50]–[51]. In [50], the authors studied MIMO antennas based on the theory of CMs to enhance port isolation for mobile communications. Using a similar approach, [51] presented a two-port structure with high isolation for mobile communications. They used tapered slots fed by microstrip lines instead of coupling elements. Moreover, some researchers are interested in MIMO techniques in the HF band for large electromagnetic wavelengths [52]–[53].

1.2.4 Distributed Transmit Beamforming

Various techniques have been recently to radiate coherently toward a desire target by employing a power distribution system [24], [54]–[55]. These techniques generally are implemented for long distance communication links between nodes (transmiter and receiver). The distributed beamforming can be used with proper weighting elements to act as an antenna array [24]. However, each node requires a precise phase delay and amplitude attenuation

for proper coherent distribution [56]. Researchers have overcome this issue by introducing digital synchronization methods capable of reducing phase difference between the nodes [26], [29]. Some of these methods are receiver-coordinated explicit-feedback [57], one-bit feedback [29], primary-secondary [26], collective ad-hoc [58], round-trip [59], and two-way synchronization [25]. However, most of synchronization methods explicitly depend on a feedback from the receiver to effectively synchronize the radios. In some cases, the dependency on the receiver creates problems when the signal is lost, and causes significant errors [26]. This problem can be avoided by considering the synchronization methods that practically are independent of the receiver. A synchronization with this quality would be very helpful for warfare implementations where the antennas cannot use enemy feedback to establish effective synchronization between the nodes. It should be noted that, primary-secondary method totally depends on the primary, but it can be easily implemented for cases where the signal is not received in order to maintain previous configuration [26]. Also, using time-slotted method with a pre-synchronization step would be ideal for those receiver independent cases. Furthermore, the implementation of the distributed transmit beamforming in the HF band will be ideal when using multiple military platforms at long distances to improve antennas radiation efficiency.

1.3 Proposed Solutions

1.3.1 Platform-Based, Electrically-Small HF Antenna With Switchable Directional Radiation Patterns

A platform-based, ESAs operating in the HF band with switchable directional radiation patterns in the azimuth plane is presented. The antenna is designed to exploit three orthogonal characteristic modes of a mid-size, ground-based platform. Two of the modes have orthogonal, figure-eight-shaped radiation patterns and the third has an omni-directional pattern along the azimuth plane. Electrically-small coupling elements along with passive feeding

and matching networks are designed to excite each mode purely with minimal coupling to the others. We demonstrate that the radiated fields of these antennas can be properly combined to generate cardioid-shaped radiation patterns in the azimuth plane whose directions of maximum radiations can be oriented towards the front, back, and the two sides of the vehicle. This antenna system can generate such directional radiation patterns with front-to-back ratios better than 15 dB over the frequency range of 6 to 24 MHz. A 1:35 scaled-model prototype of this antenna was fabricated and experimentally characterized. Measurement results of the scaled model are consistent with the simulation results of the full-scale platform and demonstrate the efficacy of the proposed design approach.

1.3.2 Capacity Analysis of Ship-to-Shore HF MIMO Systems Employing a Single-Hop Ionospheric Channel

We examine the channel capacity of a ship-to-shore high-frequency (HF) multiple-input multiple-output (MIMO) communication system that uses a near vertical incident skywave (NVIS) between the transmitter and the receiver. The channel capacity is studied using an in-house developed algorithm that takes the characteristic modes of a sea-based platform as transmitters and two orthogonal dipoles at shore as receivers. Our analytic model takes into account the polarization and spatial diversity of transmitters and receivers, as well as the statistical behavior of the ionosphere in response to the ordinary and extraordinary modes of propagation. Our objective is to maximize the channel capacity by exciting a set of characteristic modes on a fairly large stealth ship. We designed passive matching network to properly excite the desired characteristic modes on the ship. We demonstrate that the radiation fields of these antennas can be properly combined to obtained large channel capacity for NVIS communications. This antenna system is capable of maintain the channel capacity across the entire NVIS frequencies. A 1:310 scaled-model prototype of the platform including the antennas was fabricated and experimentally characterized. Measurement results of the scaled model are consistent with the simulation results of the full-scaled platform and

demonstrate the efficacy of the proposed design approach for channel capacity optimization of large platforms.

1.3.3 Future Work

Last aim involves the experimental validation of a time synchronization for distributed transmit beamforming in the HF band. We propose a distributed transmit beamforming using a principal-secundary synchronization method without any dependency on the receiver antennas target. The system would need a reduction in the transmitted phase error between transceivers by reducing the time differences between them using a GPS module as external oscillator for each transceiver. We are also interested on the case where the nodes are not in their line of sight. In real scenario for militarily applications, most of the transceivers are not directly in line of sight of the entire network even if the nodes are static or dynamic (like a moving platform).

Chapter 2

Platform-Based, Electrically-Small
HF Antenna With Switchable
Directional Radiation Patterns

2.1 Introduction

Directional antennas operating in the high-frequency (HF) band (3–30 MHz) are widely used in numerous military applications, such as long-range communications, electronic warfare (EW), and direction finding [1]-[4]. The use of directional antennas allows for focusing the radiated energy to desired directions while decreasing radiation towards unwanted directions. This improves the performance of a communication or an EW link, reduces interference, and reduces the probability of detection in military communications. The wavelengths in the HF band range from 100 m at 3 MHz to 10 m at 30 MHz. Therefore, conventional antennas operating in the HF band must be physically large to achieve directional radiation patterns. However, in many applications, such as those involving deploying antennas on moving military platforms, the space for accommodating the antennas is constrained [5]–[8]. Standalone electrically-small antennas with directional radiation characteristic (such as Huygens source antennas) have been demonstrated at higher RF and microwave frequencies [60]–[61]. However, similar to other electrically-small antennas, due to the limited dimensions, these Huygens source antennas suffer from narrow bandwidth and low radiation efficiency [9]–[11]. In addition, when these designs are scaled down to the HF band, the physical sizes of the antennas will be large enough that the interactions between the antennas and its supporting platforms cannot be ignored and will likely significantly impact the performance of the antenna.

To address some of these challenges, various techniques have been reported to use the large metallic platforms on which the antennas are mounted as the main radiator [7], [12]–[16]. Many of these techniques use the theory of characteristic modes (CMs) to design platform-based antennas that efficiently excite the CMs of the platform to achieve enhanced radiation. In [38]–[40], the authors examined the types and locations of the antennas that can effectively excite the CMs of the platform. These papers followed a similar analysis procedure of performing CM analysis first and then placing a monopole-/loop-type antenna

at locations with large change/current density of the CMs to excite the desired mode. Using a similar approach, other platform-based antennas with enhanced bandwidths have also been reported. In [13], multiple CMs of the platform were excited with a single antenna to enhance the bandwidth of an electrically-small VHF antenna. In [13], a single CM of the platform was efficiency excited with multiple antennas distributed across it to achieve bandwidth enhancement. The CM theory has also been used to manipulate the shape of the radiation patterns of antennas. In [14], this concept was used to design a null steering antenna. In [15], the authors reported a four-element, platform-based antenna array that can excite different pure CMs of an unmanned aerial vehicle with dimensions comparable to the wavelength. Due to the moderate platform size, however, these CMs have primarily omni directional patterns. In [16], multiple pure CMs of a mid-size airplane were excited and used to perform direction finding at the HF band. While the patterns of excited CMs of this work show directional characteristics at higher HF frequencies, this directionality is a consequence of the large electrical dimensions of the platform as opposed to a design feature. A shipborne antenna that can synthesize a broadside beam by exciting multiple significant CMs of a large ship was reported in [17]. However, the efficacy of this method strongly depends on having a long platform with dimensions of at least a few wavelengths. Therefore, this approach can hardly be used for generating both broadside and end-fire directional patterns when applied to a platform that is less than a wavelength long.

In this paper, we present a platform-based antenna array that can achieve switchable, directional radiation patterns by exciting and combining the CMs of a mid-size ground vehicle at the HF band. Specially, we used the Amphibious Assault Vehicle (AVV) as a representative platform and excite its CMs that have intrinsic omni-directional and figure-eight-shaped radiation patterns using electrically-small coupling elements mounted on the platform. Subsequently, cardioid-shaped radiation patterns are generated by combining a figure-eight-shaped and an omni-directional pattern with the same magnitude and phase, as shown in Fig. 2.1. With combining different CMs, the maximum radiation direction can

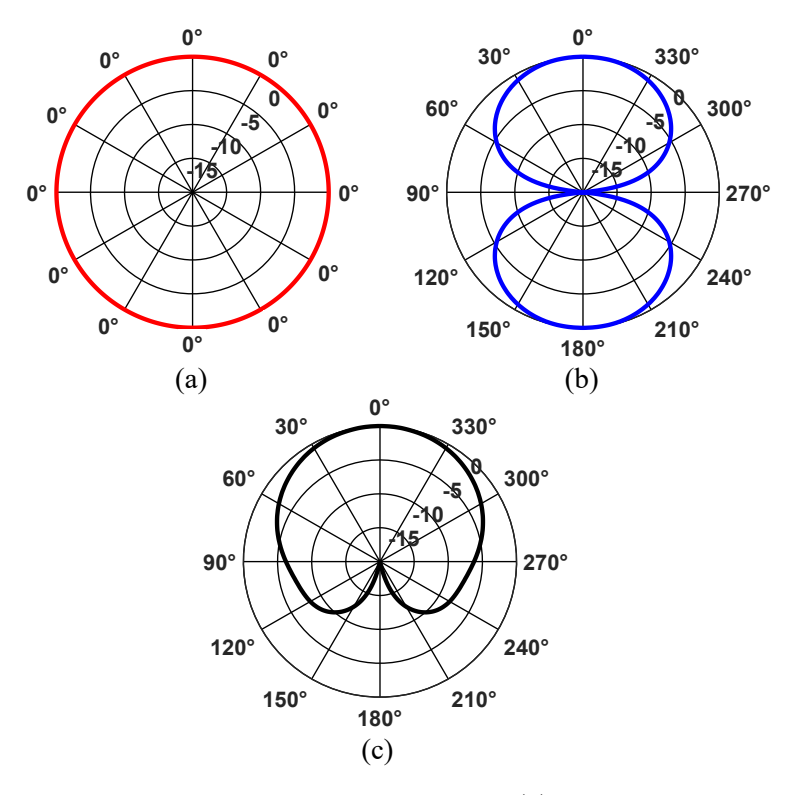


Figure 2.1: Generation of a cardioid-shaped radiation pattern. (a) An omni-directional radiation pattern. (b) A figure-eight-shaped radiation pattern. (c) A cardioid-shaped radiation pattern generated by combining the omni-directional pattern with the figure-eight-shaped pattern.

be switched to four directions with 90° separation between them in the azimuth plane. The achieved front-to-back ratio of the cardioid-shaped patterns is larger than 15 dB over the frequency range of 6–24 MHz by using a suitable feed network. A 1:35 scaled model prototype was fabricated and characterized at three representative frequencies over the operating frequency band. The measurement and simulation results agree well and demonstrate that switchable, directional radiation patterns with high front-to-back ratio can be achieved by exciting the CMs of a mid-size ground-based platform in the HF band.

2.2 Antenna Design

The proposed platform-based antenna is designed based on a simplified model of the AAV with dimensions of 7.54 m \times 3.2 m \times 2.76 m (L \times W \times H) [62]. During the design process, the platform was considered to be placed on top of an infinite perfect electric conductor

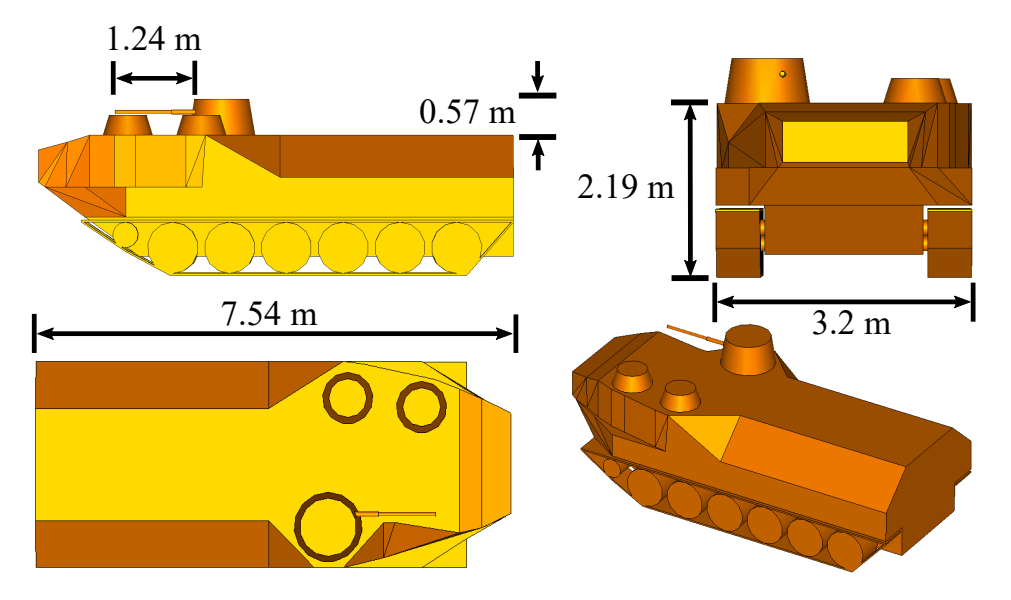


Figure 2.2: Topology and dimensions of the platform used for the design presented in this work.

(PEC) ground plane. Fig. 2.2 shows the detailed dimensions of the AAV platform used in the simulation analysis.

2.2.1 The Characteristic Mode Analysis of the Platform

The theory of CM for conducting bodies was first introduced by Garbacz [30] and later refined by Harrington and Mautz [31]. The CMs of the platform and their associated current distributions can be obtained numerically for conducting bodies. These modal current distributions are dependent on the shape and size of the object. A mode is considered to be significant if its modal significance (MS) value is larger than 0.7 at the operating frequency and an MS value of 1 indicates a resonant mode [8], [34]. Modes with higher MS values contribute more to the radiation process and can be excited more efficiently.

The design process of the proposed platform-based antenna starts by examining the CMs of the platform. For each mode, the surface current distribution, radiation patterns, and the modal significance (MS) value are examined. Fig. 2.3 shows the modal significance values of the first three modes of the AAV platform as a function of frequency. These simulation results are obtained using the CM solver of the commercial software FEKO [63]. The electric surface current distribution of these three modes and their associated radiation patterns, at

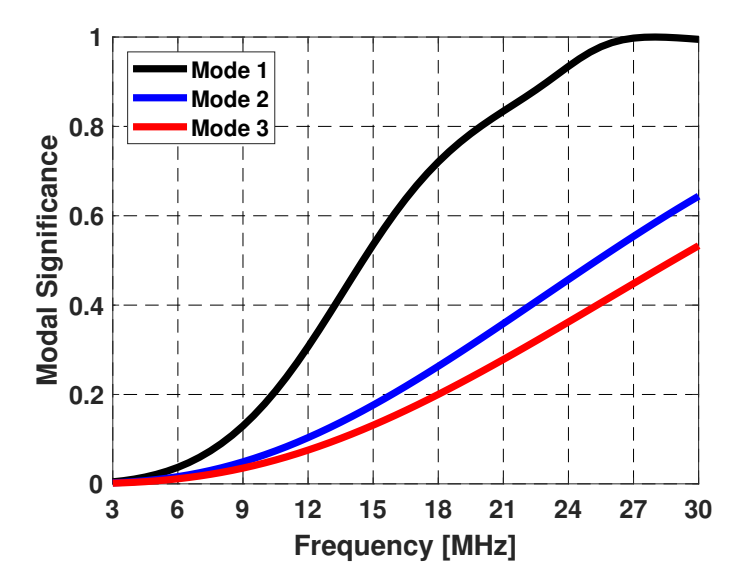


Figure 2.3: Simulated modal significance values of the first three modes of the AAV platform shown in Fig. 2.2 when the platform is mounted on an infinite PEC ground plane.

12.5 MHz, are shown in Fig. 3.3. Observe that Mode 1 is a vertically-polarized mode with an omni-directional radiation pattern in the azimuth plane with a null on the z-axis. Therefore, Mode 1 acts as a vertical electric monopole over an infinite PEC ground. Meanwhile, as shown in Figs. 3.3(b) and 3.3(c), Modes 2 and 3 act as two orthogonal vertical loops over an infinite PEC ground, which generate figure-eight-shaped radiation patterns in the azimuth plane. These modes both have vertically-polarized radiation patterns along the azimuth plane as well. Consequently, combining the radiation patterns of these modes is possible and by properly combining them, cardioid-shaped radiation patterns may be obtained.

A cardioid-shaped radiation pattern can be achieved by combining Mode 1 and Mode 2 with equal magnitudes and phases, resulting in a maximum radiation towards the front of the platform. On the other hand, if Modes 1 and 2 are combined with equal magnitudes and 180° phase difference, a cardioid-shaped radiation pattern with a maximum toward the rear end of the platform will be generated. Similarly, combining Mode 1 with Mode 3 would generate cardioid-shaped radiation patterns with maximum radiation direction pointing towards left and right of the platform in the azimuth plane. These four independent radiation patterns achieve directional radiation patterns around the platform covering the entire 360° of the

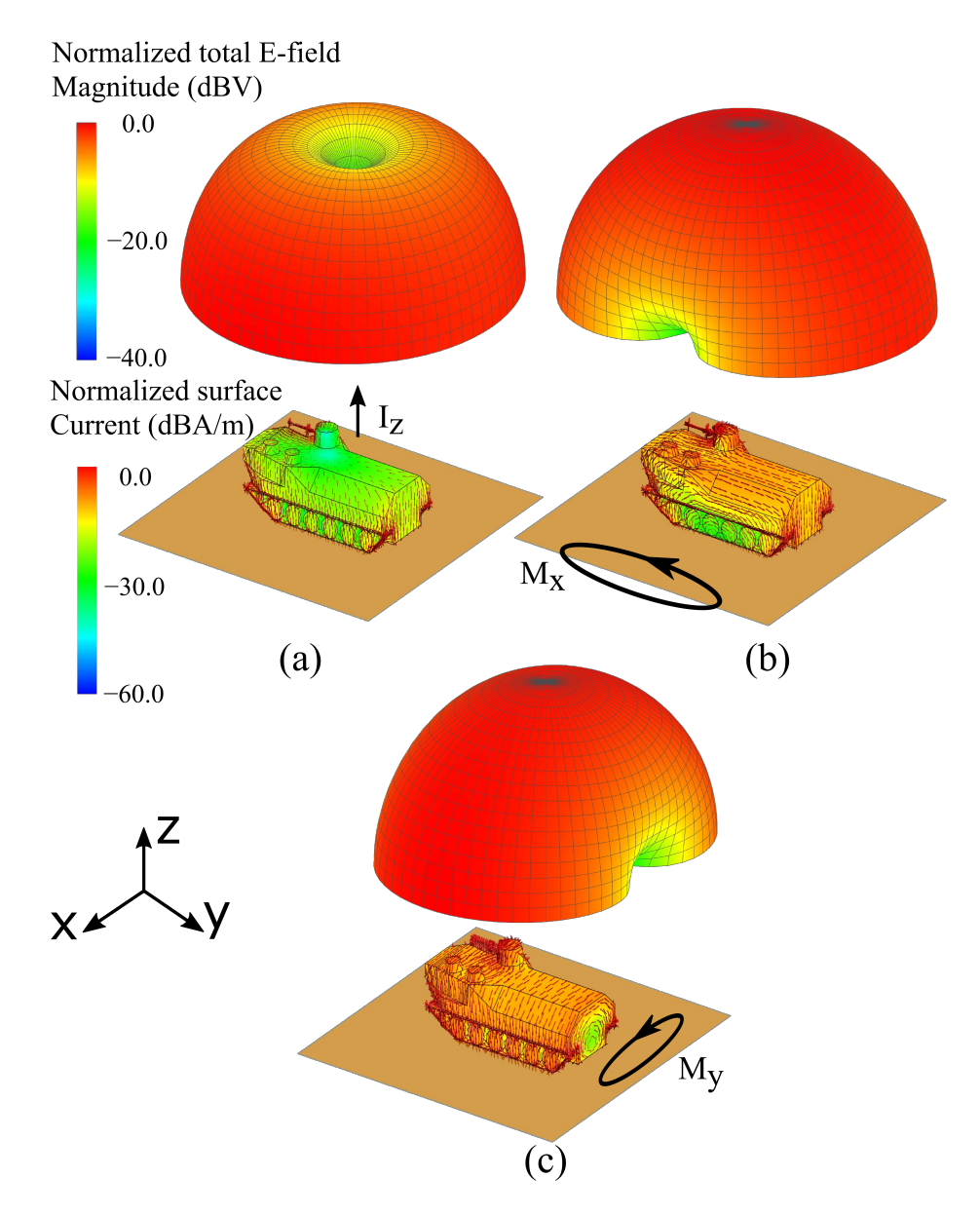


Figure 2.4: Simulated normalized radiation patterns and surface current distributions of the first three characteristic modes of the platform on an infinite PEC ground plane at 12.5 MHz. (a) Mode 1, (b) Mode 2, (c) Mode 3.

azimuth plane.

2.2.2 Designing Coupling Structures

The characteristic mode analysis presented in the previous section demonstrates that modes with radiation characteristics suitable for generating cardioid-shaped radiation patterns in the azimuth plane are available. To do this, however, coupling structures capable of exciting these modes need to be designed. Previous studies have demonstrated that characteristic modes of the platform can be excited with ESAs or coupling elements mounted on the platform [12]-[16]. Such coupling structures can be either capacitive (e.g., small dipoles) or inductive (e.g., small loops) respectively referred to as capacitive and inductive coupling elements (CCEs and ICEs). We use basic capacitive and inductive coupling elements in this design as opposed to self-matched elements such as those reported in [64]-[65]. This choice is motivated by the fact that these coupling elements are used to excite the platform modes over a wide frequency range. Self-matched elements (e.g., an inverted-F antenna) can be designed to operate at a single frequency without an external impedance matching network. However, when these antennas are made electrically small (as is the case at HF frequencies), their bandwidth would be severely limited. Therefore, operating them at frequencies other than their self-matched frequency requires an external impedance matching networks similar to those that would be needed when simple CCEs or ICEs are used. Therefore, their use in the present application where the antennas have to be tuned to work over a wide range of frequencies does not offer any advantages. Furthermore, self-match for inductive coupling elements will be more complicated on the platform with such space constrains.

Examining the current distribution of Mode 1 of the platform shown in Fig. 3.3(a) reveals that this mode has the characteristics of a vertical monopole antenna. To excite this mode, CCEs can be placed at locations where the surface electric current density of the mode attains its minimum value (the surface charge density of the mode is maximum). Alternatively, the mode can be efficiently excited with an ICEs by placing the coupling element at a location where the surface current density is maximum [40]. Meanwhile, the surface current distributions of Mode 2 and Mode 3 resemble those of two orthogonal vertical loops as shown in Figs. 3.3(b) and 3.3(c). Similar to the previous case, these modes can be excited either with capacitive or inductive coupling elements mounted at suitable locations on the platform.

Following these design guidelines, Mode 1 was excited by using two L-shaped monopoles

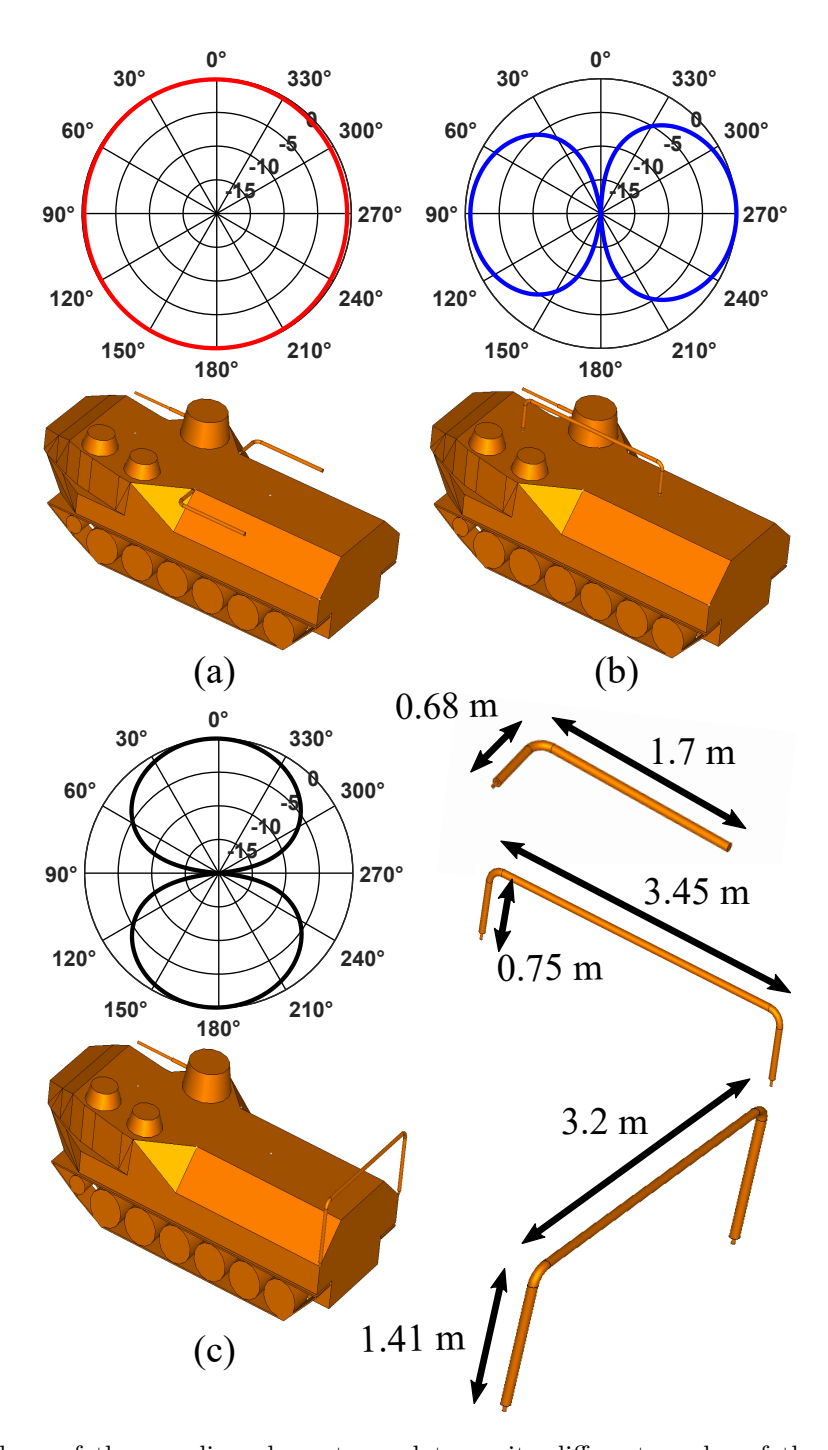


Figure 2.5: Topology of the coupling elements used to excite different modes of the platform and the normalized radiation patterns that they generate. The platform is mounted over an infinite PEC ground plane. (a) Two L-shaped monopoles fed with the same excitation coefficient are used to excite Mode 1. (b) One half-loop antenna, placed on the top surface of the platform is used to excite Mode 2. (c) One half-loop antenna, placed on top rear edge of the platform is used to excite Mode 3. All the coupling elements are designed with a copper tube with a diameter of 71.8 mm.

acting as CCEs located on top of the platform as shown in Fig. 2.5(a). In this arrangement, the planes of the L-shaped monopoles are parallel to the ground plane. This arrangement for the monopoles allows for efficiently exciting the desired mode while maintaining a low profile and thus a reduced visual signature for the antennas. The width of the monopoles is 0.81 m which provides the maximum distance between the feed point and the platform body without horizontally protruding out of the platform's boundaries. The overall length of the monopole is 1.84 m, which corresponds to an electrical dimension of $0.0184\lambda_0$ at 3 MHz (λ_0 is the free space wavelength). Mode 1 can also be excited using a single element located at the center of the platform. However, for the application at hand, two other modes need to be excited as well. Therefore, to better accommodate the antennas that will be used to excite these modes, two monopoles are used symmetrically on each side of the platform to excite Mode 1. Both Mode 1 coupling elements are excited with equal magnitudes and phases. This symmetric deployment of the monopoles helps reduce the mutual coupling between the antennas used to excite different modes of the platform.

Mode 2 is excited with a vertical half loop along the platform length as shown in Fig. 2.5(b). This mounting location is selected for two primary reasons. First, the surface current density of the mode attains its maximum on the top surface of the vehicle. Secondly, other mounting locations in the front and back of the vehicle are not suitable from a practical point of view. Specially, antennas mounted on the leading edge (front surface) of the vehicle are susceptible to damage and those mounted on the rear side (the back surface perpendicular to the ground) interfere with the primary function of the vehicle, since the vehicle's doors are located on the rear side. Additionally, positioning of this coupling element along the center axis of the vehicle (along the y axis) minimizes the mutual coupling between this coupling element and the other coupling elements used to excite Modes 1 and 3. The length and width of the half-loop were selected considering a linear dimension of an electrically-small loop with a circumference smaller than $\lambda/10$ (10 m) at the lower end of the HF band. First, we fixed the height of the half loop to 0.75 m, which is higher than the vehicle's main gun turret.

Secondly, we determined the length of the loop by gradually increasing it and observing its impact on the shape of the radiation patterns across the desired frequency band of operation. A length of 3.45 m (0.0345 λ_0 at 3 MHz) was found to be the largest length that would not deteriorate the desired figure-eight-shaped radiation pattern at the upper end of the HF band due to the increased electrical dimensions. Also, the length of the Mode 2 half loop impacts the mutual coupling between this coupling element and the monopoles collectively used to excite Mode 1. Fig. 2.5(b) shows the topology of the coupling element used to excite Mode 2 and its normalized radiation pattern along the azimuth plane at 12.5 MHz. Finally, another half loop is used to excite Mode 3 of the platform as shown in Fig. 2.5(c). This coupling element is mounted on the back edge of the platform and is positioned to be symmetric with respect to the other coupling elements. The surface current distribution of Mode 3 (shown in Fig. 3.3(c)) reveals that this location is indeed a suitable mounting location for placement of an ICE intended to excite Mode 3. Furthermore, placement of the antenna at this location does not interfere with the practical operations of the vehicle and allows for minimizing the mutual coupling between this coupling element and those used to excite Modes 1 and 2 of the platform. The length of the half loop used to excite Mode 3 was selected to be the same as the maximum width of the platform. The height of Mode 3 loop was selected based on the same criterion used to determine the height of Mode 2 half loop. However, because of the structural bend on the top surface of the vehicle on its right and left rear sides, Mode 3 half loop has a side length of 1.41 m.

2.2.3 Cardioid-Shaped Pattern Generation Using Excited Platform Modes

The coupling elements designed in the previous section are used to generate the desired cardioid-shaped radiation pattern in the azimuth plane. To examine the capability of this system in producing cardioid-shaped radiation patterns, the entire antenna system is simulated. Fig. 2.6 shows the platform with all the designed coupling elements. The two L-shaped

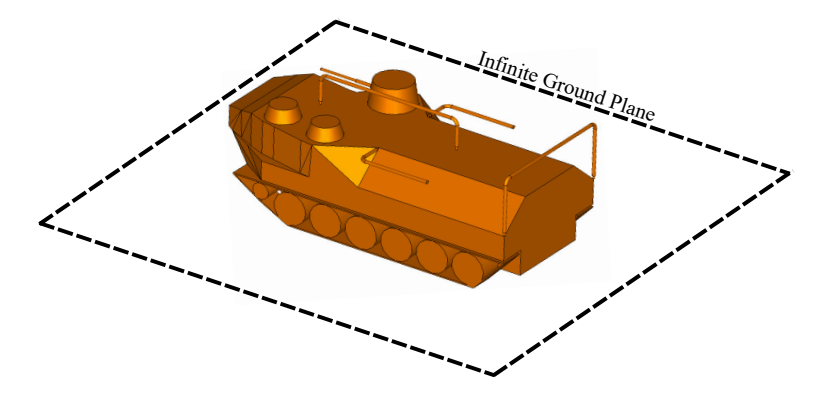


Figure 2.6: Final topology of the platform and the coupling elements mounted on it.

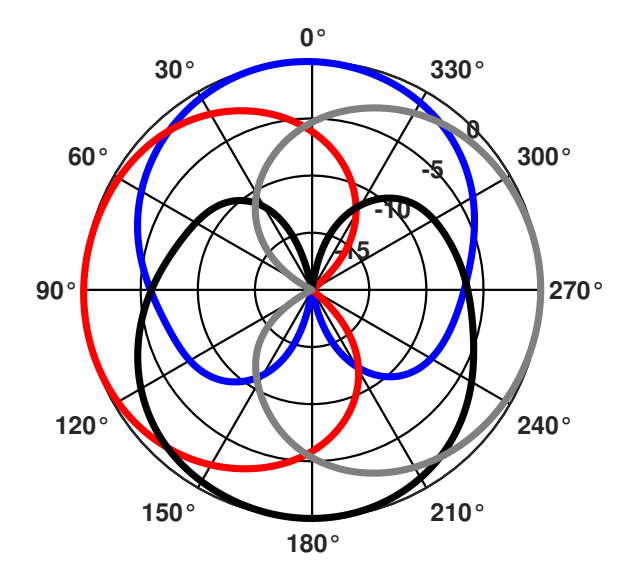


Figure 2.7: Normalized cardioid-shaped radiation patterns, at 12.5 MHz, generated by the platform-based antenna system shown in Fig. 2.6.

monopoles are fed in phase with equal magnitudes between each L-shaped monopole. Each of the two half loops is excited at its both ends differentially (i.e., with the same magnitude and with 180° phase difference). This feeding arrangement for each loop ensures that figure-eight-shaped radiation patterns with deep nulls can be achieved.

The cardioid-shaped radiation pattern can be achieved by combining an omni-directional radiation pattern with a figure-eight-shape radiation pattern. Both radiation patterns need to be excited with equal magnitudes and equal (or 180° different) phases to provide cardioid-shaped radiation patterns with peaks directed towards the desired direction and nulls exactly in the opposite direction. Fig. 2.7 shows the cardioid-shaped radiation patterns at 12.5 MHz

when different pairs of the coupling elements shown in Fig. 2.6 are exited properly. The proper excitation magnitude and phase of each coupling element can be achieved using either a passive or an active feed network.

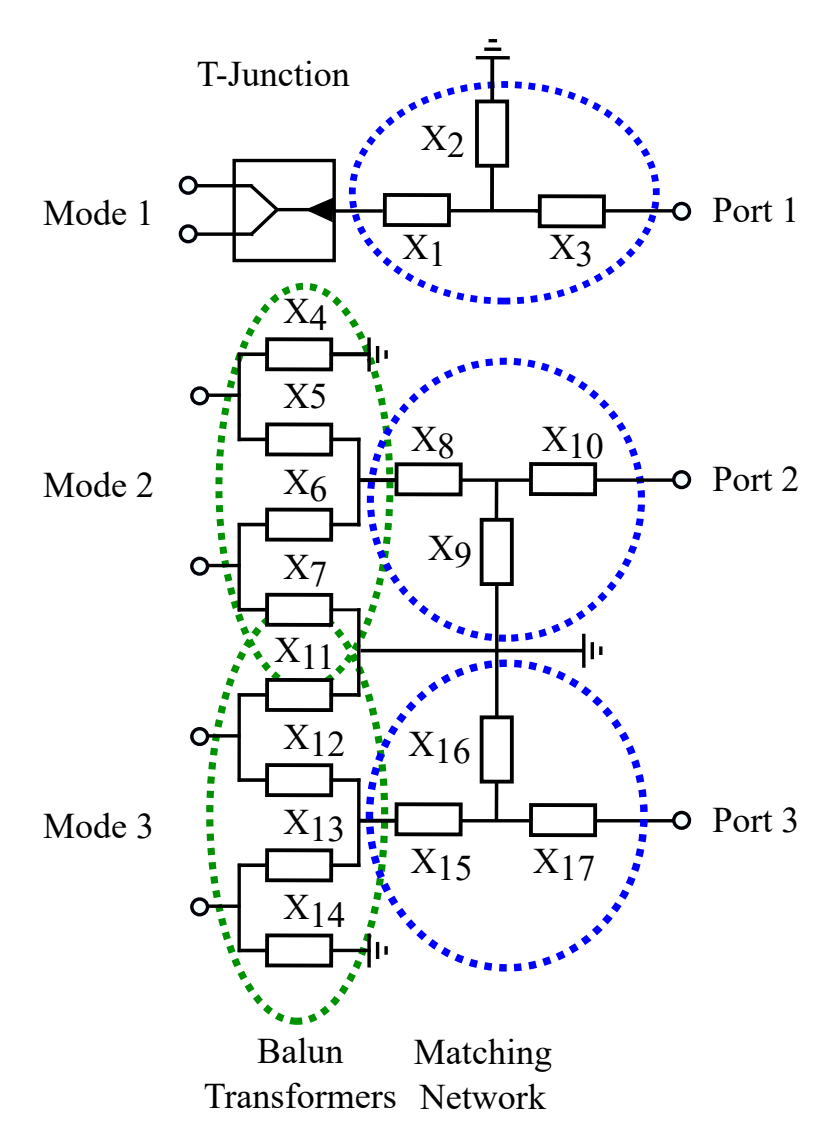


Figure 2.8: Topology of the passive feeding and matching networks used in conjunction with the coupling elements shown in Fig. 2.6.

2.2.4 Feed Network Design

Since the coupling elements are electrically small at HF frequencies, they are not impedance matched to 50 Ω . Moreover, to achieve the desired cardioid-shaped radiation patterns, the coupling elements must be excited with appropriate complex excitation coefficients. There-

fore, an external feeding and matching network should be used in conjunction with each coupling element. Fig. 2.8 shows the topology of the feed and matching network. The matching networks shown in Fig. 2.8 are T-shaped and use three reactive elements. However, in practice only two of these reactive elements are needed to impedance match the antenna at each frequency. The series element used in each network may change as frequency changes. This results in L-shaped matching network with series-element first or shunt-element first configuration at different frequencies. This way, the T-shaped matching networks shown in Fig. 2.8 may be used to match the impedance of the antennas across the entire band of operation. The capacitive coupling elements used to excite Mode 1 are fed in phase with a T-junction power divider. Following the T-junction, a matching network is used to achieve an input impedance of 50 Ω at Port 1. Meanwhile, each of the inductive coupling elements (for exciting Mode 2 and Mode 3) should be excited differentially on its both ends. This is accomplished using a 1:1 lumped-elements transformer. Following the transformer, a matching network is used to match the input impedance of each antenna to 50 Ω at Ports 2 and 3. Table 3.1 provides the total simulated efficiency of the excited modes, and the loss from each source. The sources of loss include the lossy metal material used to build the platform, the ground plane, the feed network, and the lumped elements in the feed and matching circuits. The material of the ground plane was assumed to be a good conductor similar to copper. The shape of the radiation pattern obtained when each half loop is excited is impacted by the lumped-element baluns but not by the matching networks. Therefore, to achieve the desired radiation patterns and impedance matching at the same time, it is important to first adjust the 180° transformers to secure symmetric, figure-eight-shaped radiation patterns, and subsequently determine the components values of the impedance matching networks.

Table 2.1
Simulated loss of each source and total efficiency of the excited modes for the full-scale platform at 12.5, 18, and 21 MHz.

Frequency	Modes	Lossy Metal [dB]	Ground [dB]	Microstrip Lines [dB]	Lumped Elements [dB]	Total Efficiency [dB]
	1	0.34	0.53	1.93	0.65	-2.47
$12.5~\mathrm{MHz}$	2	0.90	0.85	0.77	1.31	-1.56
	3	0.22	0.20	1.10	0.79	-1.70
	1	0.02	0.08	1.60	0.04	-2.05
$18~\mathrm{MHz}$	2	0.03	0.04	1.80	0.53	-1.97
	3	0.08	0.16	1.59	0.56	-1.86
	1	0.07	0.02	2.04	0.29	-2.54
$21~\mathrm{MHz}$	2	0.06	0.05	2.16	0.51	-2.29
	3	0.05	0.04	1.72	0.28	-1.92

2.3 Experimental Results

The antenna design and simulation results presented in Section 2.2 are for a full-scale AAV. However, experimentally validating these design concepts for a full-scale platform is not possible, given our available resources. Therefore, to validate the proposed concept, a scaled-model prototype using simplified model of the AAV was fabricated and characterized. In this simplified model, the wheels of the scaled-model prototype of the AAV were replaced with solid blocks. This was done to facilitate the task of metalization of the fabricated scaled-model prototype. Moreover, because the small features of the wheels are significantly smaller than the wavelength across the entire HF band, this change does not significantly impact the antenna design or expected results. Additionally, a finite-size, circular-shaped aluminum ground plane with radius of 0.41 m was used as the ground plane for the scaled model.

2.3.1 Design of the Scaled-Model Antenna Prototype

A 1:35 scaling factor was chosen based on the frequency range of our anechoic chamber. With this scaling factor, the HF band is scaled to 105–1050 MHz. Fig. 2.9(a) shows the topology of the scaled-model AAV platform with the coupling elements mounted on the finite ground plane. In the simulations of the scaled-model prototype shown in Fig. 2.9,

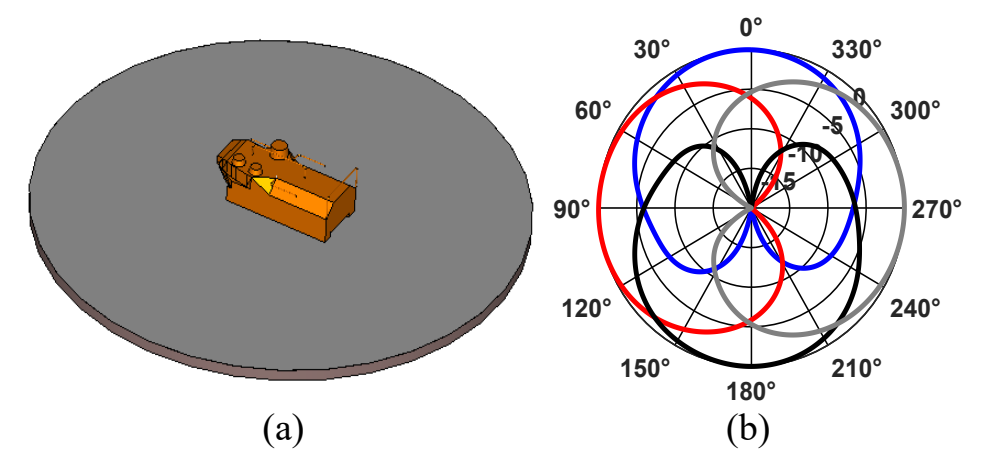


Figure 2.9: (a) A simplified scaled model of the platform on top of a circular-shaped aluminum ground plane with radius of 0.41 m. (b) Simulated normalized cardioid-shaped radiation patterns generated by this scaled-model prototype in the azimuth plane at 437 MHz.

the ground plane is assumed to be made of aluminum and the platform and the antennas mounted on it are assumed to be made of copper. The structure was simulated using fullwave electromagnetic simulations in CST Studio [66] at the frequencies 437, 630, and 735 MHz (corresponding to 12.5, 18, and 21 MHz of the full-scale platform). In these simulations, the coupling elements used to excite Modes 1, 2, and 3 were excited individually (with other elements terminated to matched loads) and the radiation patterns excited by each element were obtained. The radiation patterns were obtained considering the impact of the feed network designed to excite each element (see Fig. 2.8). In this process, the losses and the parasitics of the lumped-element components used in the feed network have been considered. These patterns were then combined with appropriate magnitudes and phases to generate the desired cardioid-shaped radiation patterns. The values of the lumped-element components used in CST simulations (to obtain the S-parameters and the radiation patterns) are shown in Table 3.2. The feed networks were simulated in Keysight's Advanced Design System (ADS) [67]. Figs. 2.10(c) and 2.10(d) show the layouts of the feed networks designed and used in the simulations. Both feed networks were designed to be fabricated on 0.813 mm thick RO4003C substrates with a dielectric constant of 3.55 and loss tangent of 0.0027. Fig. 2.9(b) shows the simulated cardioid-shaped radiation patterns obtained through this process at 437 MHz (corresponding to 12.5 MHz in the full-scale prototype). Observe that the scaled model prototype is expected to be capable of providing the same cardioid-shaped radiation patterns obtained from the full-scale model.

2.3.2 Fabrication Process

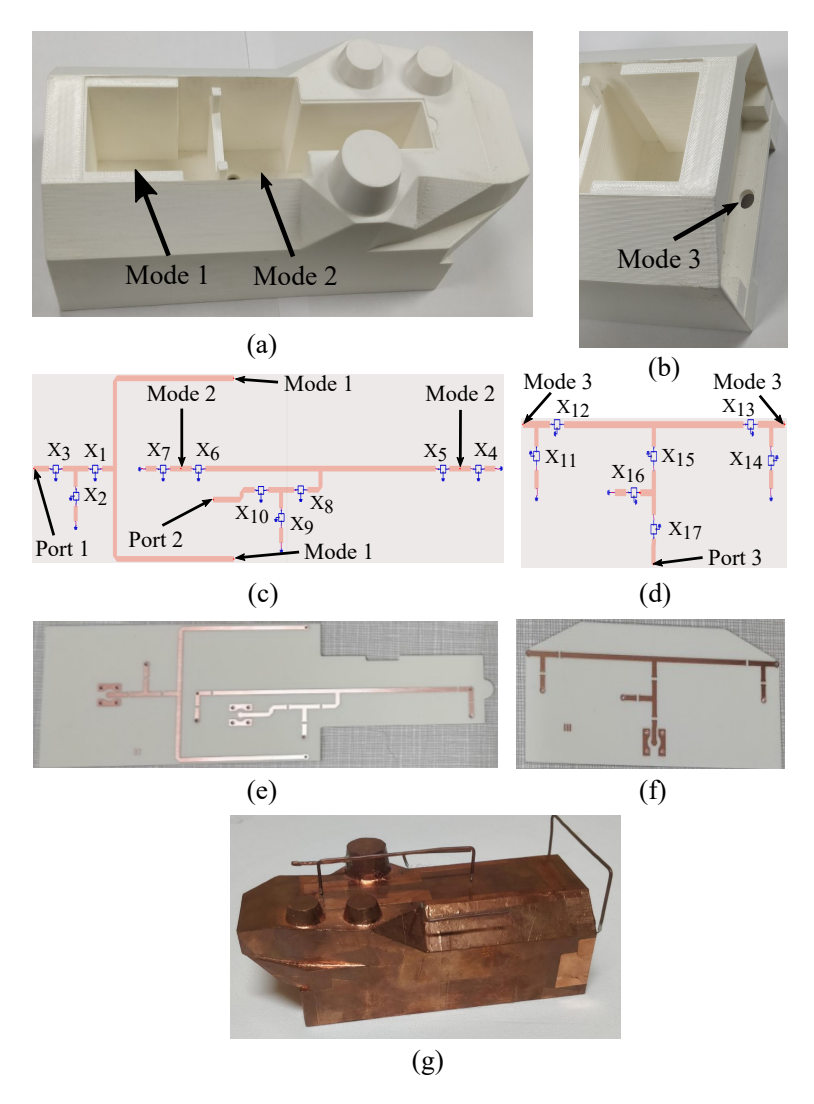


Figure 2.10: Photographs of a 1:35 scaled-model fabricated prototype and its feed network. Coaxial connectors are placed beneath the platform and connected to the feed network inside the hollow 3-D platform. (a) 3-D printed platform with interior cavities used to accommodate Mode 1 and 2 feed networks. (b) Photograph of the rear section of the 3-D printed platform showing the cavity used to accommodate the Mode 3 feed network. (c)-(f) Layout and photographs of the feed network designed to excite the different coupling elements. (g) Photographs of the assembled scaled-model prototype.

A prototype of the scaled-model platform-based antenna was fabricated using three-dimensional (3-D) printing as shown in Figs. 2.10(a) and 2.10(b). Part of the inside of

the 3-D printed model was left hollow to accommodate the placement of the feeding and matching networks. The 3-D printed model contains holes on the bottom for the coaxial cable to pass through and connect to the PCB with the feeding network. All of the exterior of the fabricated 3-D scaled model was covered with copper tape including the bottom of the model. The cavities contain small frame holders on their edge to support the fabricated PCBs containing the feed networks.

The feed network designed in ADS presented previously is shown in Figs. 2.10(c) and 2.10(d). The PCB layout presented contains the feed and matching networks used to excite their corresponding coupling elements. The feed networks used to excite the coupling elements of Modes 1 and 2 were fabricated on the same PCB and that for Mode 3 was fabricated on a separate one. The detailed layout of the feed networks along with the relevant geometrical and physical dimensions are provided in Fig. A.1 of the Appendix A section. The PCBs are positioned in the interior of the vehicle such that the ground planes of the microstrip lines are electrically connected to the exterior metalized body of the platform. Feed through vias having diameters of 0.81 mm connected the appropriate terminals of the feed network to the feed terminals of the coupling elements. The coupling elements are implemented using 12 gauge copper wires with diameters of 2.05 mm. The feed network is implemented on a 0.813 mm thick RO4003C dielectric substrate with dielectric constant of 3.55 and loss tangent of 0.0027. The values of the lumped-element components used in the fabricated feed networks are provided in Table 3.2. Figs. 2.10(e) and 2.10(f) show photographs of the fabricated feed networks (without lumped-element components). The values of the lumped-element components used in the feed network are slightly different from those used in the simulations. These differences are attributed to the tolerances involved in fabricating the scaled-model prototype as well as slight differences between the simulated and fabricated models (e.g., using copper tape in the fabricated prototype versus solid sheet assumed in the simulated prototype, etc.). Despite these differences, one can easily compensate for these effects by changing the values of the lumped-element components used in the feed network as we have done.

Table 2.2 Component values of the matching networks of the simulated and fabricated scaled model at $437,\,630,\,$ and $735\,$ MHz.

	Frequency	437	MHz	630	MHz	735	MHz
	Type	Simu.	Measu.	Simu.	Measu.	Simu.	Measu.
	X_1	2.3 nH	4.7 nH	18.8 pF	2.8 pF	8.2 pF	6.8 pF
Mode 1	X_2	24 pF	24 pF	15.3 pF	14.7 pF	10 pF	10 pF
	X_3	Short	Short	Short	Short	Short	Short
	X_4	47 nH	47 nH	33 nH	33 nH	22 nH	22 nH
	X_5	1.5 pF	1.5 pF	1.8 pF	1.8 pF	1.5 pF	1.5 pF
	X_6	47 nH	47 nH	33 nH	33 nH	22 nH	22 nH
Mode 2	X_7	1.5 pF	1.5 pF	1.8 pF	1.8 pF	1.5 pF	1.5 pF
	X_8	6.0 nH	5.6 nH	Short	Short	Short	2.2 pF
	X_9	22 pF	23.3 pF	36 nH	12 nH	18 nH	4.7 nH
	X_{10}	Short	Short	1.5 pF	1.8 pF	1.5 pF	Short
	X_{11}	68 nH	68 nH	33 nH	33 nH	20 nH	20 nH
	X_{12}	1.8 pF	1.8 pF	0.8 pF	0.8 pF	1.2 pF	1.2 pF
	X_{13}	68 nH	68 nH	33 nH	33 nH	20 nH	20 nH
Mode 3	X_{14}	1.8 pF	1.8 pF	0.8 pF	0.8 pF	0.8 pF	0.8 pF
	X_{15}	39 pF	10 pF	Short	Short	1.3 pF	Short
	X_{16}	15 pF	10 pF	4.7 pF	10 nH	8.5 nH	6.0 nH
	X_{17}	Short	Short	15 nH	2.2 pF	Short	1.8 pF

2.3.3 Measurement Results

The assembled prototype is shown in Fig. 2.10(g). It was put on top of a circular-shaped ground plane with a diameter of 0.82 m, made out of aluminum. The S-parameters of the fabricated prototype were measured in the vicinity of 437, 630, and 735 MHz (corresponding to 12.5 MHz, 18 MHz, and 21 MHz for the full-scale model). Fig. 3.9 shows the measured S-

parameters in the vicinity of the 630 MHz. Observe that the input reflection coefficients are below -10 dB for each antenna and the mutual coupling between the three coupling elements remains below -20 dB. Similar results were observed for the measurements performed in the vicinity of 437 and 735 MHz. Table 2.3 summarizes the fractional bandwidth of each antenna and the level of mutual coupling between them at these three frequencies over which S-parameter measurements were performed.

Table 2.3

Measured S-parameters of the fabricated scaled-model prototype in the vicinity of 437, 630, 735 MHz.

Frequency	Modes	 FBW (%)	Mutual Coupling (dB)				
Trequency	Modes	TDW (70)	S_{1X}	S_{2X}	S_{3X}		
	1	1.42	_	-41.5	-40.8		
$437~\mathrm{MHz}$	2	0.84	-41.0	_	-41.4		
	3	0.87	-40.9	-41.0	_		
	1	0.85	_	-22.3	-29.1		
$630~\mathrm{MHz}$	2	0.93	-22.3	_	-36.5		
	3	1.43	-29.2	-36.4	_		
	1	0.65	-	-17.5	-29.0		
$735~\mathrm{MHz}$	2	1.10	-17.5	_	-31.1		
	3	1.27	-28.9	-31.2	_		

The realized gain patterns (both magnitudes and phases) of the fabricated prototypes were measured with a multi-probe near-field system (SATIMO StarLab). The measurements were performed by exciting one antenna at a time (when the other two were terminated with 50 Ω). Through this process, complete three dimensional realized gain pattern (magnitudes and phases for both θ and ϕ polarizations) for each mode was obtained at three frequencies of 437, 630, and 735 MHz. The measurement results were post processed in Matlab [68]. Lastly, to generate the desired cardioid-shaped radiation patterns, the measured patterns of two modes (Modes 1 and 2 or Modes 1 and 3) were combined with appropriate complex weighting coefficients that ensures that the fields radiated by each mode has the same magnitude and

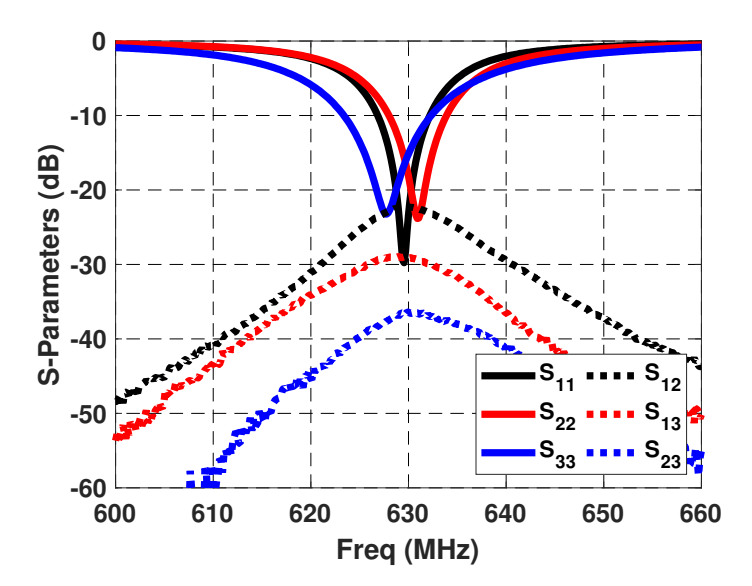


Figure 2.11: Measured S-parameters of the fabricated scaled-model prototype in the vicinity of 630 MHz (corresponding to 18 MHz for the full-scale prototype).

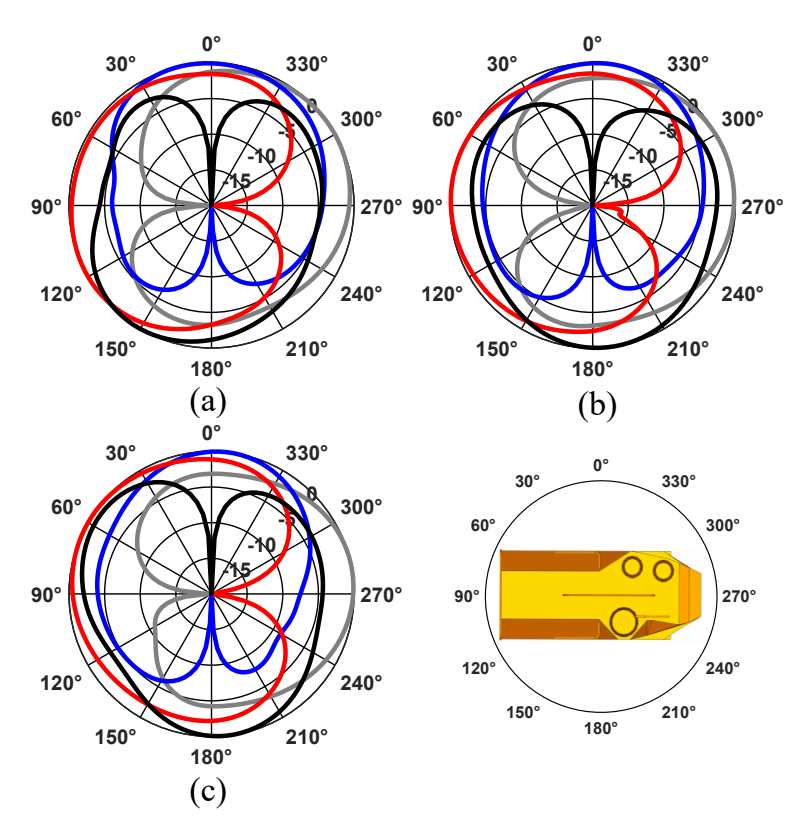


Figure 2.12: Measured normalized, cardioid-shaped radiation patterns of the scaled-model prototype shown in Figs. 2.9 and 2.10. (a) 437 MHz (12.5 MHz). (b) 630 MHz (18 MHz). (c) 735 MHz (21 MHz).

phase along the direction of maximum radiation. This process emulates an active feed network that can provide the required amplitude and phase of the excitation of each element which results in the desired cardioid-shaped radiation pattern. One potential implementation of such an active feed network for a directional HF transmitter is shown in Fig. A.2 of the Appendix A section. Fig. 2.12 shows the cardioid-shaped radiation patterns obtained using this process at 437, 630, and 735 MHz (corresponding to 12.5, 18, and 21 MHz for the full-scale model). The weighting coefficients used to obtain these results are presented in Table 2.4. Each cardioid-shaped radiation pattern has the beam pointing towards a desired direction with a null in the opposite direction and has a front-to-back ratio larger than 15 dB. Comparing Figs. 2.9 and 2.12(a), it can be observed that the measured and simulated radiation patterns are similar. The minor differences observed between the two can be primarily attributed to the presence of a large feeding cable connected to the platform, which was not modeled in the simulations. Lastly, Table 2.5 presents the measured realized gain values of the cardioid-shaped radiation patterns shown in Fig. 2.12.

Table 2.4

Excitation coefficients of ports for generating cardioid-shaped radiation patterns in the azimuth plane. The orientations are based on the platform shown in Fig. 2.12.

Excitation Coefficients (Simulation)				Excitation Coefficients (Measurement)					
Frequency	Mode	0° (Left)	90° (Back)	180° (Right)	270° (Front)	0° (Left)	90° (Back)	180° (Right)	270° (Front)
	1	1∠120°	1∠-90°	1∠-60°	1∠90°	1.7∠−40°	1.35∠107.5°	1.83∠120°	1.93∠−68.5°
$437~\mathrm{MHz}$	2	_	1∠0°	_	1∠0°	_	1∠0°	_	1∠0°
	3	0.75∠0°	_	0.75∠0°	_	1∠0°	_	1∠0°	_
	1	0.65∠105°	1∠0°	0.65∠−75°	1∠180°	0.3∠23.5°	1.9∠−165°	0.35∠−126°	1.8∠1°
$630~\mathrm{MHz}$	2	_	0.75∠0°	_	0.75∠0°	_	1∠0°	_	1∠0°
	3	1∠0°	_	1∠0°	_	1∠0°	_	1∠0°	_
	1	0.75∠−50°	1∠−20°	0.75∠0°	1∠160°	0.2∠48.5°	3.9∠139°	0.2∠231°	1.1∠−52.5°
$735~\mathrm{MHz}$	2	_	0.75∠0°	_	0.75∠0°	_'	1∠0°	_	1∠0°
	3	1∠0°	_	1∠0°	_	1∠0°	_	1∠0°	_

The total measured and simulated radiation efficiencies of each mode of the scaled-model prototype are reported in Table 3.3. Several factors contribute to reducing the radiation efficiencies of the antennas. The first factor is the small electrical dimensions of the antennas, which results in reduction of their radiation resistances and increasing their feed-point quality factors (Q). The second factor is the losses of the feeding and matching network used for each coupling element. These losses are likely the most important factor contributing to

Table 2.5

Measured realized gain of the Cardioid-Shaped radiation patterns for the scaled-model prototype shown in Figs. 2.9 and 2.10.

Beam Angle	0°	90°	180°	270°
437 MHz	-9.6 dBi	-7.5 dBi	-10.3 dBi	-9.4 dBi
$630~\mathrm{MHz}$	-1.2 dBi	-7.9 dBi	-1.7 dBi	-8.8 dBi
$735~\mathrm{MHz}$	-1.7 dBi	-9.2 dBi	-1.2 dBi	-10.2 dBi

Table 2.6 Simulated and measured total efficiencies of the coupling elements used to excite different modes.

Frequency	Mode	1 (dB)) Mode 2 (dB		Mode	3 (dB)
rrequency	Sim.	Meas.	Sim.	Meas.	Sim.	Meas.
437 MHz	-8.4	-9.5	-12	-10.5	-5.6	-6.3
$630~\mathrm{MHz}$	-5.2	-5.7	-3.3	-5.3	-4.5	-6.3
$735~\mathrm{MHz}$	-2.9	-4.2	-2.8	-4.5	-3.8	-6.8

the reduced overall efficiency of the antenna. This is due to the concept of matching loss magnification, which refers to the reduction in the transmission efficiency between the source and the antenna caused by the multiple reflections that exist between a high-Q ESA and its matching circuit (see [69], pp. 46-48). The higher the Q factor of an antenna is, the higher the matching loss magnification will be. Other minor factors such as surface roughness and finite conductivity of the copper tapes and aluminum sheets used in the fabrication of the prototype and the ground plane are potential contributing factors too, albeit to a lesser extent.

2.4 Conclusion

We reported the design and experimental characterization of a platform-based, HF antenna system capable of producing directional radiation patterns in the azimuth plane. The proposed design is based on exciting three orthogonal characteristic modes of a mid-sized ground-based platform. One of these modes has an omni-directional radiation pattern and the other

two have orthogonal, figure-eight-shaped radiation patterns. By properly combining these patterns, cardioid-shaped radiation patterns whose directions of maximum radiations can be directed towards front, back, and both sides of the platform can be obtained. Suitable coupling elements along with their associated feed and impedance matching networks were designed to excite each of these three characteristic modes. Full-wave electromagnetic simulations of the full-scale model of the proposed system were performed and demonstrated that the system can generate directional radiation patterns across the frequency range of 6–24 MHz within the HF band.

To experimentally verify the operation of the proposed antenna, a 1:35 scaled-model prototype along with the required baluns and matching networks were fabricated and experimentally characterized. Both S-parameter and radiation pattern measurements were performed in the vicinity of 437, 630, and 735 MHz (corresponding approximately to 12.5, 18, and 21 MHz for the full-scale model). Note that the losses of the full-scaled model are lower than those of the scaled-model prototype because the lumped elements used in the impedance matching network have significantly lower losses at the HF band. Measurement results demonstrated that good impedance matching can be achieved and despite being closely spaced and sharing the same platform, the mutual coupling between the different coupling elements is small (below -20 dB). Furthermore, it was demonstrated that by combining the radiation patterns of the different modes, cardioid-shaped radiation patterns with front-to-back ratios better than 15 dB can be obtained across this frequency band. Similar to any other high-Q electrically-small antenna the overall antenna efficiency is adversely impacted by the antenna size as well as the losses of the balun and the matching networks used to feed the antenna. Even small losses of the matching network can be amplified significantly due to the larger difference between the input and output VSWRs of the matching network (i.e., matched loss magnification [69]). This factor in conjunction with the small radiation efficiency of the antennas are the two primary factors contributing to the relatively low measured radiation efficiencies.

Chapter 3

Capacity Analysis of Ship-to-Shore
HF MIMO Systems Employing a
Single-Hop Ionospheric Channel

3.1 Introduction

Near-vertical incident skywave (NVIS) antennas operates in the high-frequency (HF) band (2–10 MHz) range and they are highly useful for beyond line-of-sight (BLOS) communications [41]–[42]. The NVIS propagating signal between the transmitter and the receiver is reflected on the F-layer of the ionosphere (i.e., a single-hop path) [43]. However, due to the large wavelengths of electromagnetic waves at HF band, its physically challenging design antennas on moving platforms [13], [16]. Furthermore, the narrow bandwidth of HF channels limits data transfer rate transmitted over a single channel. Therefore, architectures for multiple-input multiple-output (MIMO) communication system are being highly study [70]–[71].

To address some of these challenge, researchers has exploited the two propagating modes of the ionosphere, the ordinary (O) and the extraordinary (X) from the F-layer, which are orthogonal polarized. [44]. The two wave interact with the ionosphere and bounce back to the receiver as a multipath fading wave [72]. However, most of the wave losses occur on the D-layer and E-layer. In [45]–[46] the ionosphere refraction index has been estimated using integral models of multipath. These papers successfully models the fading wave absorption due to the D-layers based on the frequency of operation. Furthermore, in [47], a method to predict the maximum usable frequency with respect of the path length for the propagating wave. The model take into consideration the mode of reflection on each layer and their corresponding maximum communication distance. However, the ionospheric channels are changing with time, geolocation, the plasma levels, and temperature [48]. Consequently, if the ionospheric channel is restricted frequency band limited and the transmission communication is for a short period, a tap-gain model can represent any ionosphere hopping. This model is call the Watterson model represented as a fading Gaussian scatter channel model. In [73], they formulate a 2×2 NVIS channel matrix for collocated orthogonal transmitter/receivers dipoles above earth with orthogonal diversity and representing the ionospheric complex numbers for the two F-layers. More importantly, the approach was limited to a predetermine MIMO size, antenna configuration, and ionosphere complex values. On moving platform the size is limited and mounting orthogonal dipoles operating a lower NVIS frequencies could results in large space consumption. Using the characteristic mode (CM) of the platform will provide better radiation patterns with physical small antennas capable for fitting over a the moving platform [17], [74].

In this paper, we present a ship-to-shore HF MIMO communication link using a single-hop channel and examine the impacts of polarization diversity on the MIMO channel capacity. Specially, we used the Zumwalth-Destroyer battleship as a representative platform for the transmitters and excite items CMs for maximize channel capacity to two orthogonal horizontal dipole above dry earth at shore as receivers. We consider the designed of platform-based antenna antennas that excite an optimum subset of the CMs of the platform to maximize channel capacity [16]. The transmitter were generated using resonators mounted on the platform. Subsequently, two orthogonal radiation patterns were generated using two resonators exciting multiple characteristic modes of the platform. The maximum radiation of the multiple characteristics modes of the platform were directed toward the sky for the NVIS communication. The designed resonators were able to maintain their directionality across the NVIS band by using suitable feed network. A 1:310 scaled model prototype was fabricated and characterized at three representative frequencies covering the entire NVIS frequency band. The measurement and simulation results agree well and demonstrate the channel capacity optimization can be achieved by exciting the CMs of the water-based platform in the HF band.

3.2 Single-Hop, Ionospheric MIMO Channel Modeling

The ionospheric NVIS model follows reference [73] where discusses a specific case of a 2×2 NVIS MIMO channel for collocated transmitters and receivers. On our model we build upon the derivation in [73] and generalizes it so as to include antennas configuration larger than

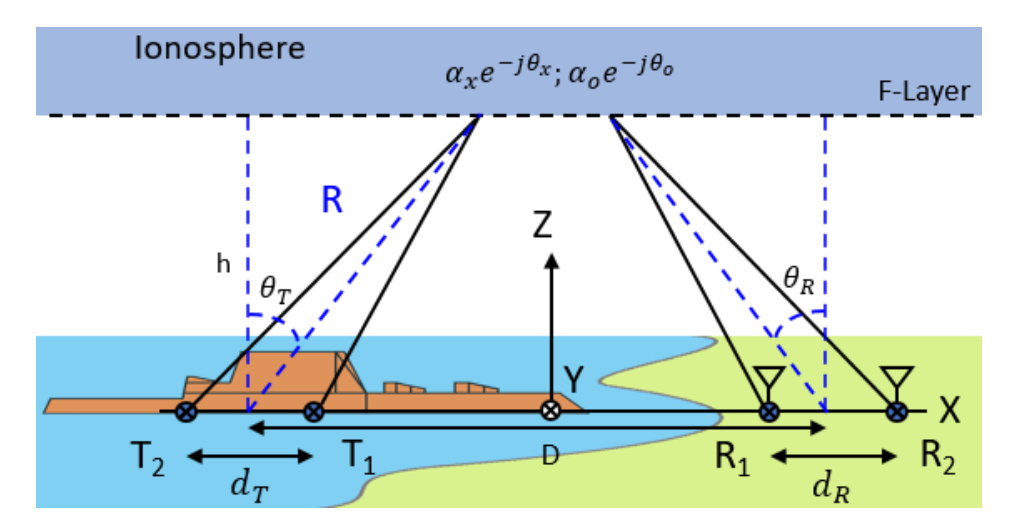


Figure 3.1: Schematic illustrating a single-hop, ship-to-shore ionospheric channel with multiple inputs and multiple outputs.

two as well as the effects of spatial diversity and the statistical behavior of the ionosphere in the model. Fig. 3.1 shows a ship-to-shore, single-hop ionospheric link for a 2 \times 2 MIMO system, but the derivation applies to any $M \times N$ MIMO scenarios.

3.2.1 Propagation Modeling

The model consider multiple transmitters $(T_1, T_2, ..., T_N)$ over a platform located on salty water and multiple receivers $(R_1, R_2, ..., R_M)$ located on a base station at shore with a separation of D. Transmitters has a separation between them defined as d_T while the receivers has a separation defined as d_R . The receivers are predetermine as two orthogonal horizontal dipoles above dry earth at shore.

Taking into consideration the signals of the transmitters are the electric fields at the far field; the field phasor radiated by the first antenna T_1 with the field pattern g_{T_1} at the departure elevation angle ε_d is:

$$\overline{E}_{T_1} = s_1 g_{T_1}(\varepsilon_d) e^{-j[k\hat{r}_1 \cdot r_1']} \hat{x}$$
(3.1)

where $g_{T_1}\varepsilon_d$ are the far-field electric fields at the particular angle of departure.

$$g_{T_1}\varepsilon_d = E_{T_1}(\theta_T, \phi_T) \tag{3.2}$$

where $r'_1 = \frac{d}{2}\hat{x}$ is the unit vector along the transmitters, s_1 denotes the low-pass equivalent signal, and \hat{r}_1 is the far-field unit vector directed toward the ionosphere defined as

$$\hat{r}_1 = \sin(\theta_T)\cos(\phi_T)\hat{x} + \sin(\theta_T)\sin(\phi_T)\hat{y} + \cos(\theta_T)\hat{z}$$
(3.3)

Using the equations (3.2) and (3.3), (3.1) can be written as

$$\overline{E}_{T_1} = s_1 E_{T_1} e^{j\left[\frac{k_0 d}{2} sin(\theta_T)\right]} \hat{x} \tag{3.4}$$

Since the interaction of the wave with the ionosphere will slip linear polarization into a sum of two orthogonal circular polarization equation (3.4) can be written as

$$\overline{E}_{T_1} = \frac{1}{2} s_1 E_{T_1} P_{T_1} (\hat{x} - j\hat{y}) + \frac{1}{2} s_1 E_{T_1} P_{T_1} (\hat{x} + j\hat{y})$$
(3.5)

where E_{T_1} is a linear polarization of the transmitter 1 split into right hand circular polarized (RHCP) and left hand circular polarized (LHCP). The decomposition help with the reflection of the ionosphere F_1 and F_2 layer. Similarly, for the second transmitter T_2 :

$$\overline{E}_{T_2} = s_2 E_{T_2} e^{-j[\frac{k_0 d}{2} \sin(\theta_T)]} \hat{y}$$
(3.6)

Since $r'_2 = -\frac{d}{2}\hat{x}$, $E_{T_1}(\theta_T, \phi_T)$ is the far-field electric fields at the particular angle of departure for the second transmitter, and s_2 denotes the low-pass equivalent signal of the second transmitter.

$$\overline{E}_{T_2} = \frac{j}{2} s_2 E_{T_2} P_{T_2} (\hat{x} - j\hat{y}) - \frac{j}{2} s_2 E_{T_2} P_{T_2} (\hat{x} + j\hat{y})$$
(3.7)

Representing both signals as a matrix for the transmitted case and assuming signals normalization $(s_1, s_2) = 1$,

$$\overline{E}_T = \frac{1}{2} \begin{bmatrix} E_{T_1} P_{T_1}(\hat{x} - j\hat{y}) & j E_{T_2} P_{T_2}(\hat{x} - j\hat{y}) \\ E_{T_1} P_{T_1}(\hat{x} + j\hat{y}) & -j E_{T_2} P_{T_2}(\hat{x} + j\hat{y}) \end{bmatrix}$$
(3.8)

Since the NVIS channels consist of only one-hop, we assume a complex response h_x and h_o . Ionosphere statistical complex coefficients for the two modes are:

$$\mathbf{H_{ox}} = \begin{bmatrix} \alpha_x e^{-j\theta_x} & 0\\ 0 & \alpha_o e^{-j\theta_o} \end{bmatrix}$$
 (3.9)

where gains α_x and $alpha_o$ and phase shifts θ_x and θ_o of the paths are statistically provided and discussed on the next section.

Now studying the waves arriving at the receiver experience antenna far-field electric fields and polarizations:

$$\overline{E}_R = \begin{bmatrix} E_{R_1} P_{R_1} \hat{x} & E_{R_1} P_{R_1} \hat{x} \\ E_{R_2} P_{R_2} \hat{y} & E_{R_2} P_{R_2} \hat{y} \end{bmatrix}$$
(3.10)

where P_{R_1} stand for $e^{j[\frac{k_o d}{2}sin(\theta_R)]}$ and $P_{R_2} = e^{-j[\frac{k_o d}{2}sin(\theta_R)]}$.

The MIMO channel matrix is define as $H = \overline{E}_R \mathbf{H_{ox}} \overline{E}_T$ Reducing the equation we will end up with equation 3.11

$$\mathbf{H}_{2\times2} = \frac{1}{2} \begin{bmatrix} E_{R_{1n}} P_{R_1} E_{T_{1n}} P_{T_1} T_+ & -j E_{R_{1n}} P_{R_1} E_{T_{2n}} P_{T_2} T_- \\ j E_{R_{2n}} P_{R_2} E_{T_{1n}} P_{T_1} T_- & E_{R_{2n}} P_{R_2} E_{T_{2n}} P_{T_2} T_+ \end{bmatrix}$$
(3.11)

where
$$T_+ = (\alpha_x e^{-j\theta_x} + \alpha_o e^{-j\theta_o})$$
 and $T_- = (\alpha_x e^{-j\theta_x} - \alpha_o e^{-j\theta_o})$.

Following same procedure of the simple case, we can extended it for a general $M \times N$ MIMO channel with arbitrary antenna polarizations. The channel matrix will result in a channel matrix as given by (3.12). Here, $T_{M,N} = a_{M,N}T_+ + jb_{M,N}T_-$, $a_{M,N} = \Re(e^{j\Psi_{M,N}}) = cos(\Psi_{M,N})$, and $b_{M,N} = \Im(e^{j\Psi_{M,N}}) = sin(\Psi_{M,N})$. The Ψ angle is provided by the polarization difference between the transmitter N and the receiver M. On the previous formulation of the 2×2 we study two orthogonal polarizations on both size. If we follow the same study with the reduced general equation, we will end up obtaining equation (3.11).

$$\mathbf{H}_{M\times N} = \frac{1}{2} \begin{bmatrix} E_{R_{1n}} P_{R_1} E_{T_{1n}} P_{T_1} T_{1,1} & E_{R_{1n}} P_{R_1} E_{T_{2n}} P_{T_2} T_{1,2} & \cdots & E_{R_{1n}} P_{R_1} E_{T_{Nn}} P_{T_N} T_{1,N} \\ E_{R_{2n}} P_{R_2} E_{T_{1n}} P_{T_1} T_{2,1} & E_{R_{2n}} P_{R_2} E_{T_{2n}} P_{T_2} T_{1,2} & \cdots & E_{R_{2n}} P_{R_2} E_{T_{Nn}} P_{T_N} T_{2,N} \\ \vdots & \vdots & \ddots & \vdots \\ E_{R_{Mn}} P_{R_M} E_{T_{1n}} P_{T_1} T_{M,1} & E_{R_{Mn}} P_{R_M} E_{T_{2n}} P_{T_2} T_{M,2} & \cdots & E_{R_{Mn}} P_{R_M} E_{T_{Nn}} P_{T_N} T_{M,N} \end{bmatrix}$$

$$(3.12)$$

3.2.2 Ionospheric Mode of Propagation

The HF ionospheric channel are non-stationary in both frequency and time, due to the ionospheric layer changing heights with time [48]. However, Watterson develop a tap-gain function capable of representing most ionosphere with a stationary ergodic statistical model by limiting the transmission time and band-limit the operational frequency. The model is represented by tap-gain function with a power spectrum of a Gaussian function define as:

$$G_i(f) = \frac{1}{A_x \sigma_x \sqrt{2\pi}} e^{\frac{-(f - f_x)^2}{2\sigma_x^2}} + \frac{1}{A_o \sigma_o \sqrt{2\pi}} e^{\frac{-(f - f_o)^2}{2\sigma_o^2}}$$
(3.13)

where A_x and A_o are the attenuation component, $2\sigma_x$ and $2\sigma_o$ are the frequency spread, and ν_x and ν_o are the frequency shifts for the two ionosphere modes (extraordinary and ordinary mode).

To compare the performance and the statistical model of each model, in [75] provided representative channel parameters to general each frequency power spectrum for each mode. The recommendation letter provides multiple set of values depending on the latitudes, conditions, and type of propagation. We generate the frequency power spectrum using the values for the NVIS wave propagation. With the power spectrum we can select a random process and is used as part of Monte-Carlo simulations to obtain the ergodic statistical capacity of the channel. The in-house algorithm flowchart along with the ionospheric modeling ergodic statistical channel capacity are explained in the Appendix B.

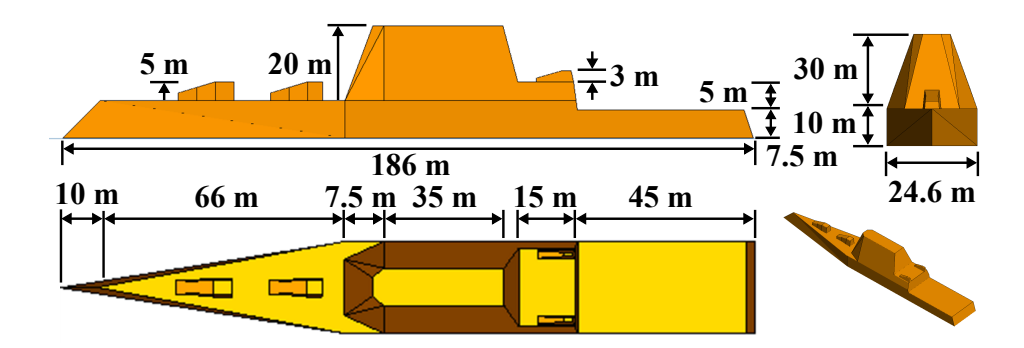


Figure 3.2: Topology and dimensions of the platform used for the design presented in this work.

3.2.3 Channel Capacity

Finally, if we assume ideal case where all the transmitter elements have equal power distribution on the channel matrix, we wont have a full rank matrix. Since we are going to study CMs of a platform as transmitters, the probability of each transmitter been nearly identical (e.g., gain, polarization) is rather impossible. However, the channel capacity of the NVIS MIMO can be calculated based on the assumption of water-filling power allocation [76]–[77],

$$C_{MIMO} = \sum_{i=1}^{U} \log_2 \left(1 + \frac{P_i^*}{N_0} \lambda_i \right) \tag{3.14}$$

where $U = min(N_t, N_r)$, N_t , and N_r being the number of transmitters and receivers, $P_i^* = (\mu - N_0/\lambda_i)^+$, λ_i being the eigenmode of the channel, and μ is chosen to satisfy the total power constrain $\sum_i = 1P_i^* = P$, and N_0 denotes noise.

3.3 Antenna Configuration

The proposed platform-based antenna is designed based on a simplified model of a battleship Zumwalt-Class destroyer (ZWD) with dimensions of 186 m \times 24.6 m \times 40 m (L \times W \times H) [78]. Note that these dimensions only consider the area outside of the sea water. The platform is considered to be placed on top of an infinite perfect electric conductor (PEC) that fairly represents the sea water surface at the HF band. Fig. 3.2 shows the detailed dimensions of the ZWD platform used in the simulation analysis.

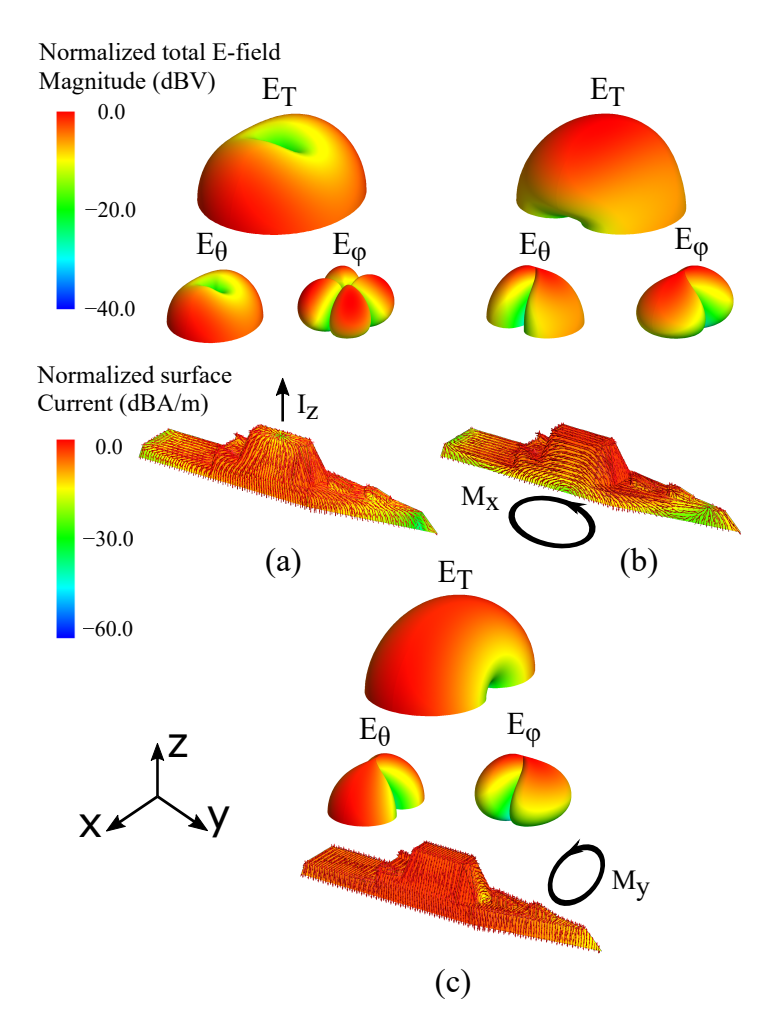


Figure 3.3: Simulated normalized radiation patterns and surface current distributions of the first three characteristic modes of the platform on an infinite PEC ground plane at 2 MHz. (a) Mode 1, (b) Mode 2, (c) Mode 3.

3.3.1 Design Procedure

In designing the proposed NVIS MIMO Channel capacity, we follow two primary design objective. First, we need to excited the entire NVIS frequencies with a minimum number of resonators. Second, we need to study all the platform's CMs combination as transmitters while receiving the data with two orthogonal dipoles horizontally place over dry earth. The CMs of the platform were obtained using the CM solver of the commercial software FEKO [63]. The CMs are combine as a subset of 2 and processed with a MatLab in-house code to study the maximum MIMO NVIS channel capacity combination [68]. To accomplish these

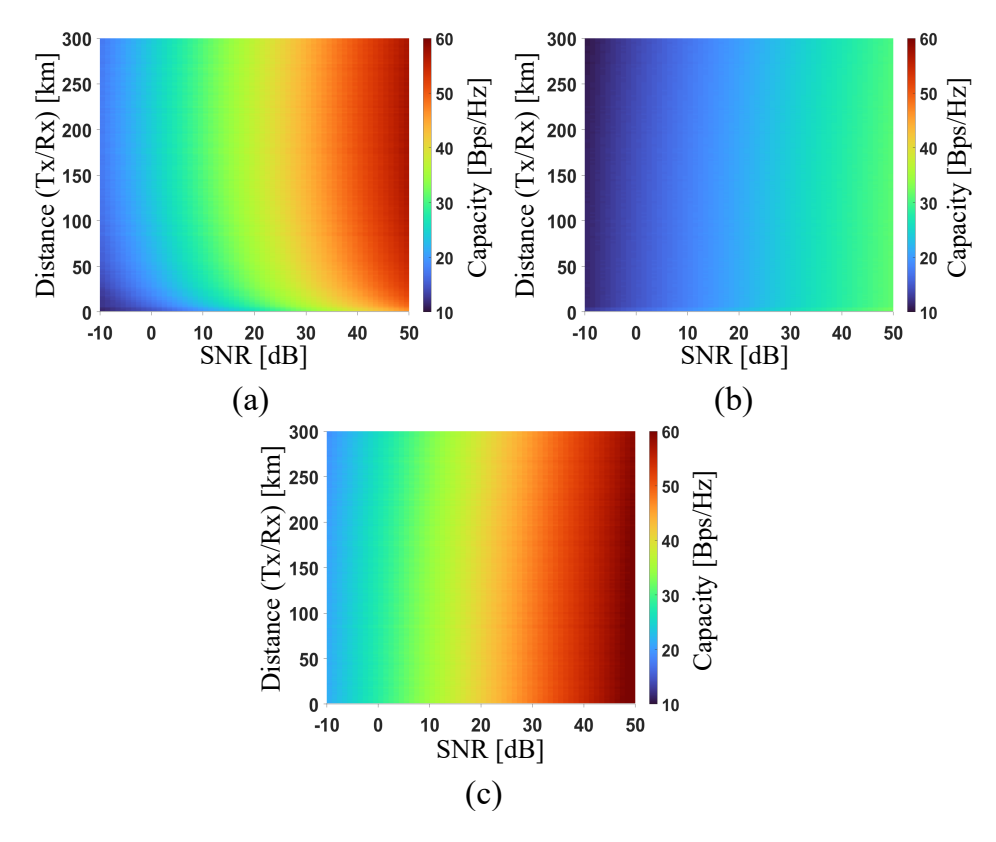


Figure 3.4: NVIS MIMO channel capacity at 2 MHz using platform's CMs for a 2×2 MIMO channel. (a) Modes 1 & 2, (b) Modes 1 & 3, (c) Mode 2 & 3.

goals, we used the theory of CMs as a tool in the design process. CMs of the platform and their associated current distributions can be obtain numerically for the conducting bodies [31]–[32]. The electric surface current distribution of these three modes and their associated radiation patterns, at 2 MHz, are shown in Fig. 3.3. However, none of them has a modal of significant larger than 0.7 at the particular frequency.

Observe that Mode 1 is a vertically-polarized mode with an omni-directional radiation pattern in the azimuth plane with a null on the z-axis. Therefore, Mode 1 acts as a vertical electric monopole over an infinite PEC ground as shown in 3.3(a). Meanwhile, as shown in Figs. 3.3(b) and 3.3(c), Modes 2 and 3 act as two orthogonal vertical loops over an infinite PEC ground, which generate perfect orthogonal radiation patterns for NVIS communications. Consequently, combining these radiation patterns we can obtain the best channel capacity using the CMs of the platform combine with the two orthogonal dipoles at the

receivers end. Fig. 3.4(a)–(b) shows a contour map for the NVIS MIMO channel capacity at 2 MHz for the transmitters combinations of Modes 1 & 2, Modes 1 & 3, and Modes 2 & 3, respectively. The figure study the channel capacity in bps/Hz when the distances between the transmitters and receivers ranges from 1 km to 300 km (ignoring the ground wave propagation cases) and the SNR in dB from 0 to 50 dB. Modes 2 & 3 are two orthogonal loops providing the best channel capacity for NVIS communications while the Modes 1 & 3 are the worst. The reason for Modes 1 & 3 be so low is because Mode 1 has partial excutation with Mode 3. Even with the water-filling distributing, the energy between the two modes is not equally distributed between each modes, instead is exciting only the best mode to maximize the NVIS MIMO channel capacity.

3.3.2 Design Coupling Structures

The CM analysis presented in the previous section demonstrates the in-house code modes combination using their radiation patterns for suitable NVIS communication. However, the best mode combination is provided when two orthogonal radiation patterns are excited. Previous studies have demonstrated that characteristic modes of the platform can be excited with simple resonators placement over a platform [38]–[39]. Such resonators structure can be either capacitive (e.g., dipoles) or inductive (e.g., loops) respectively. However, using resonators to excited particular modes of the platforms becomes very difficult at higher frequencies. The surface current at higher frequencies contain complex location to excite the ideal mode with a single resonator and end up on multiple resonators place very separated. A way to solve this problem will be exciting multiple modes with a single resonator that has a radiation pattern of interest. In our case, we would like to excite radiation patterns that has orthogonality between them and centralizing their energy toward the ionosphere, and they maintain their radiation orthogonality across the NVIS frequencies.

If we examine the current distribution to excite a platform with a mode like the one shown in Fig. 3.3(a) reveals that this mode has the characteristics of a vertical monopole antenna

at the top of the platform. Using a capacity resonator we can excite this mode by placing it at locations where the surface electric current density of the mode attains its minimum value. Alternatively, the mode can be efficiently excited with an inductive resonator by placing the resonator at a location where the surface current density is maximum. However, as shown before on fig. 3.4(a) we can have better communication for long ranges, but lower capacity at closer range. Meanwhile, the surface current distributions of Mode 2 and Mode 3 resemble those of two orthogonal vertical loops as shown in Figs. 3.3(b) and 3.3(c). Similar to the previous case, these modes can be excited either with capacitive or inductive resonators mounted at suitable locations on the platform.

Taking into consideration the platform surface current and the case where we obtain the largest channel capacity for all ranges as shown in fig. 3.4(c). This case will required orthogonal radiation patterns, which are typically excited using a half-loop resonators. The lower frequency of the NVIS channel can be excited using a single resonator for each Mode 2 and 3. However, at higher NVIS frequencies, the surface current of the platform is more distributed over the platform requiring multiple resonators to perfectly excite a single mode of the platform. Furthermore, the resonators location to excite a pure mode are distanced between them resulting on an inefficient design. For this reason, we are indeed interested on exciting multiple CMs instead of a single mode of the platform. This can be achieve by selecting all the modes with radiation along the platform and excited them with a single resonator where they share the same current distribution. Similarly, we can select all the modes with radiation across the platform and excited them with a single resonators that share same current distribution spots.

Following all this guidelines, to excite CMs with radiation patterns along the platform was used a L-shaped monopole acting as capacitive resonators located on the front center wall as shown in Fig. 3.5(a)-(b) resonator 1. This mounting location was selected because of the surface current density of the modes attain their minimum at that location for all the NVIS frequencies without interfere with primary functions of the platform (rockets, ship

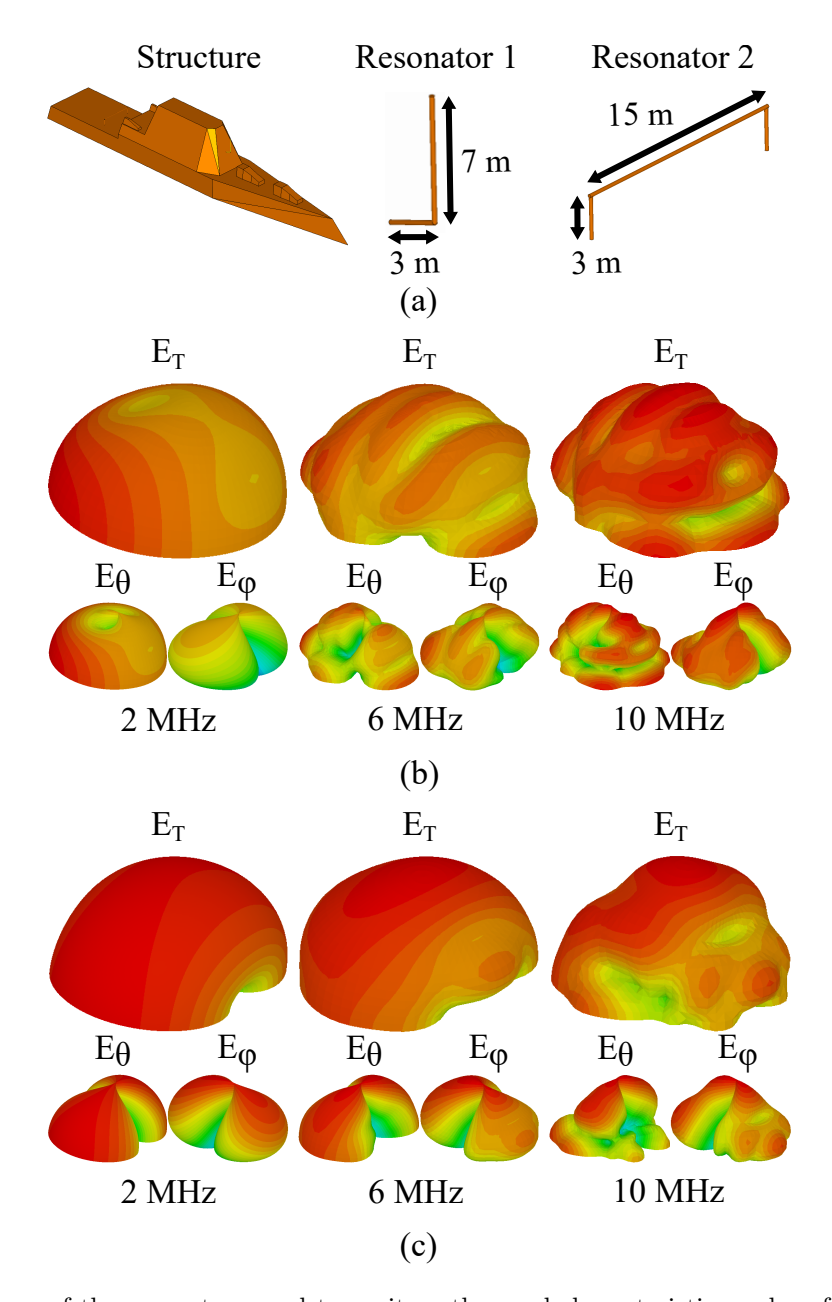


Figure 3.5: Topology of the resonators used to excite orthogonal characteristic modes of the platform and the normalized radiation patterns with their corresponding component. The platform is mounted over an infinite PEC ground plane. (a) Platform structure with each resonator dimensions. (b) Normalized radiation patterns of the resonator 1 on the NVIS frequencies. (c) Normalized radiation patterns of the resonator 2 on the NVIS frequencies.

bridge visibility, etc). Additionally, positioning of this resonator along the center axis of the vehicle orthogonal to the surface, but the other half of the L-shape monopole orthogonal to the walking ground of the ship. The overall length of the monopole is 10 m which corresponds to an electrical dimensions of $0.067\lambda_0$ at 2 MHz (λ_0 is the free space wavelength). We fixed

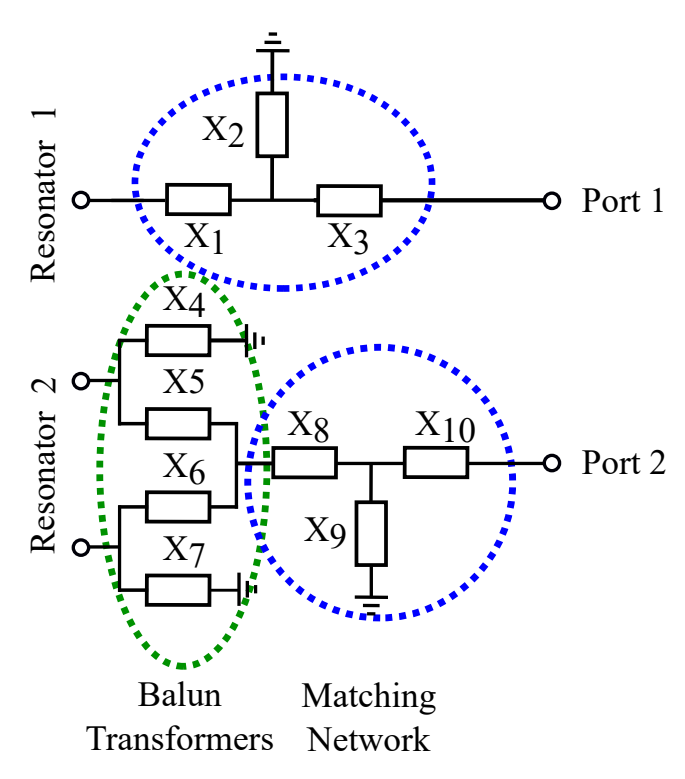


Figure 3.6: Topology of the passive feeding and matching networks used in conjunction with the coupling elements shown in 3.5

the height of the monopole to not exceed the total height of the ship's top. The resonator has a self-resonance at 7.5 MHz. The second resonator selected was a half-loop to excite CMs across the platform as shown in Fig. 3.5(a) resonator 2 with radiation patterns shown in Fig. 3.5(c). This resonator element is mounted on the back flight deck of the platform and is positioned to excited the entire NVIS frequencies. Furthermore, placement of the antenna at this location does not interfere with the practical operations of the platform as long as the ships are smaller than its height. The length of the half loop used to excite CMs across the platform was selected to be larger than the landing deck, which we end up using 15 m long. The height of the loop was selected to be 3 m based on fabrication limitations.

3.3.3 Feed Network Design

Since the resonators have self-resonance at higher end of the NVIS frequencies, they are not impedance matched to 50 Ω on the entire band. Moreover, to achieve the channel capacity improvement the data must be share between both resonators. Therefore, an external feeding

and matching network should be used in conjunction with each resonator. Fig. 3.6 shows the topology of the feed and matching network. The matching networks shown in Fig. 3.6 are T-shaped and use three reactive elements. However, in practice only two of these reactive elements are needed to impedance match the antenna at each frequency. The series element used in each network may change as frequency changes. This results in an L-shaped matching network with series-element first or shunt-element first configuration at different frequencies. This way, the T-shaped matching networks shown in Fig. 3.6 may be used to match the impedance of the antennas across the entire band of operation using a single board design. The capacitive resonator used to excite Modes along the platform required a matching network to achieve an input impedance of 50 Ω at Port 1. Meanwhile, the inductive resonator, to excite modes across the platform, should be excited differentially on its both ends. This is accomplished using a 1:1 lumped-element transformer. Following the transformer, a matching network is used to match the input impedance of each antenna to 50Ω at Port 2. Table 3.1 provides the total simulated efficiency of the resonators, and the loss from each source. The sources of loss include the lossy metal material used to build the platform, the ground plane, the feed network, and the lumped elements on the feed and matching circuits. The material of the ground plane was assumed to be a good conductor similar to copper. The shape of the radiation pattern obtained when each half loop is excited is impacted by the lumped-element baluns but not by the matching networks. Therefore, to achieve the desired radiation patterns and impedance matching at the same time, it is important to first adjust the 180° transformers to secure symmetric and subsequently determine the components values of the impedance matching networks.

Table 3.1 Simulated loss of each source and total efficiency of the excited modes for the full-scale platform at 2, 6, and 10 MHz.

Frequency	Reso.	Lossy Metal [dB]	Ground [dB]	Micro. Lines [dB]	Lum. Elem. [dB]	Total Effi. [dB]
2 MHz	1	0.007	0.027	1.284	8.743	-10.048
2 WIIIZ	2	0.347	0.032	1.503	18.601	-20.349
6 MHz	1	0.003	0.044	0.001	0.586	-0.654
O WIIIZ	2	0.006	0.012	0.460	7.679	-9.169
10 MHz	1	0.001	0.048	0.004	0.094	-0.132
10 MHz	2	0.002	0.002	0.076	0.984	-1.064

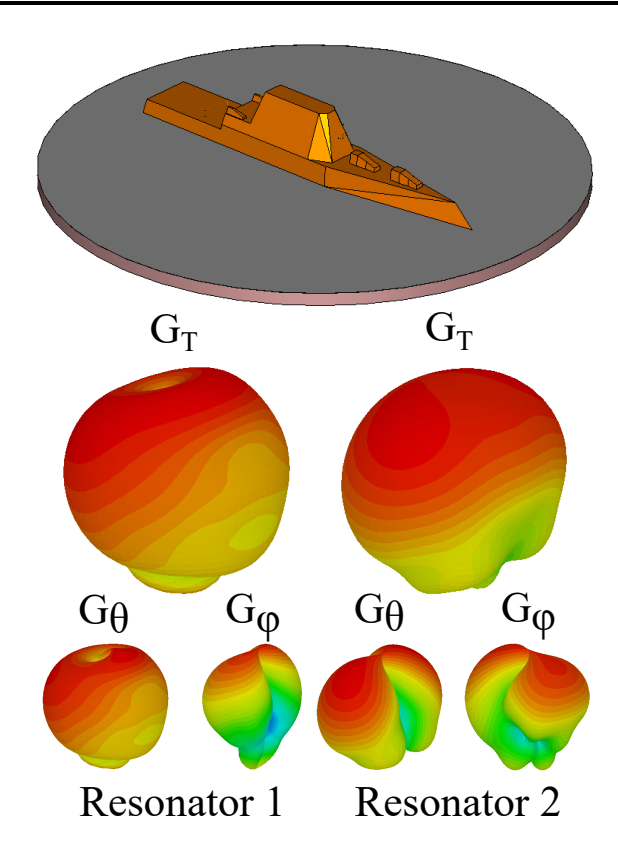


Figure 3.7: A simplified scaled model of the platform on top of a circular-shaped aluminum ground plane with radius of 0.41 m. The radiation patterns is given to 2 MHz since the ground is smaller than $\lambda/2$ for each sides.

3.4 Experimental Results

3.4.1 Design of the Scaled-Model Antenna Prototype

We fabricated and measured a 1:310 scaled version of the ZWD, which the scaled factor was chosen based on the frequency range of our near-field spherical anechoic chamber. The scaling factor of 1:310 the NVIS frequencies is scaled to 620 MHz–3100 MHz. Our near-field system can perform measurements in the 600 MHz–18 GHz frequency range and accommodate antennas with linear dimensions up to 0.82 m. Based on this, the prototype dimension is results on $0.6 \text{ m} \times 0.08 \text{ m} \times 0.13 \text{ m}$ (L × W × H) that is near the maximum size of our chamber. Then can used the rest of the space as a finite-size, circular-shaped aluminum ground plane with a radius of 0.41 m as the ground plane for the scaled model. However, reducing the size of the structure more to allocate a better grounding will result on other fabrication complications (e.g., linear dimension of the monopole resonators is 10 m scaled to 0.03 m using a scaled factor of 1:310).

Fig. 3.7 shows the topology of the scaled-model ZWD platform with the resonators mounted on the aluminum finite ground plane. In the simulations of the scaled-model prototype shown in Fig. 3.7, the ground plane is assumed to be made of aluminum on top of a cardboard and the platform and the antennas mounted on it are assumed to be made of copper. The structure was simulated using full-wave electromagnetic simulations in CST Studio [66] at the frequencies 620, 1860, and 3100 MHz (corresponding to 2, 6, and 10 MHz of the full-scale platform). In these simulations, the resonators used to excite Modes along and across the platform were excited individually (with other elements terminated to matched loads) and the radiation patterns excited by each element were obtained. The radiation patterns were obtained considering the impact of the feed network designed to excite each element (see Fig. 3.6). In this process, the losses and the parasitics of the lumped-element components used in the feed network have been considered. The values of the lumped-

element components used in CST simulations (to obtain the S-parameters and the radiation patterns) are shown in Table 3.2. The feed networks were simulated in Keysight's Advanced Design System (ADS) [67]. Both feed networks were designed to be fabricated on 0.813 mm thick RO4003C substrates with a dielectric constant of 3.6 and loss tangent of 0.0027. Fig. 3.7 shows the simulated radiation patterns obtained through this process at 620 MHz (corresponding to 2 MHz in the full-scale prototype). Observe that the scaled model prototype have energy over the ground edge since the ground is not the ideal size. However, the radiation patterns orthogonality still remains for the NVIS channel capacity.

3.4.2 Fabrication Process

A prototype of the scaled-model platform-based antenna was fabricated using three-dimensional (3-D) printing as shown in Fig. 3.8(c). Since the linear size of the platform is 0.6 m, we needed to divide the structure in two parts. Furthermore, we build a clip/slider mechanism to hold together the two ZWD parts. The part of the inside of the 3-D printed model was left completely hollow to accommodate the placement of the feeding and matching networks. The 3-D printed model contains holes on the bottom for the coaxial cable to pass through and connect to the PCB with the feeding network. All of the exterior of the fabricated 3-D scaled model was covered with copper tape including the bottom of the model as shown in Fig. 3.8. The cavities contain small frame holders on their edge to support the fabricated PCBs containing the feed networks.

The feed network designed in ADS are shown in Figs. 3.8(a) and 3.8(b) for resonator 1 and resonator 2, respectively. The PCB layout presented contains the feed and matching networks used to excite their corresponding resonator. The PCBs are positioned in the interior of the vehicle such that the ground planes of the microstrip lines are electrically connected to the exterior metalized body of the platform. Feed through vias having diameters of 0.81 mm connected the appropriate terminals of the feed network to the feed terminals of the resonators. The resonators are implemented using 21 gauge copper wires with diameters

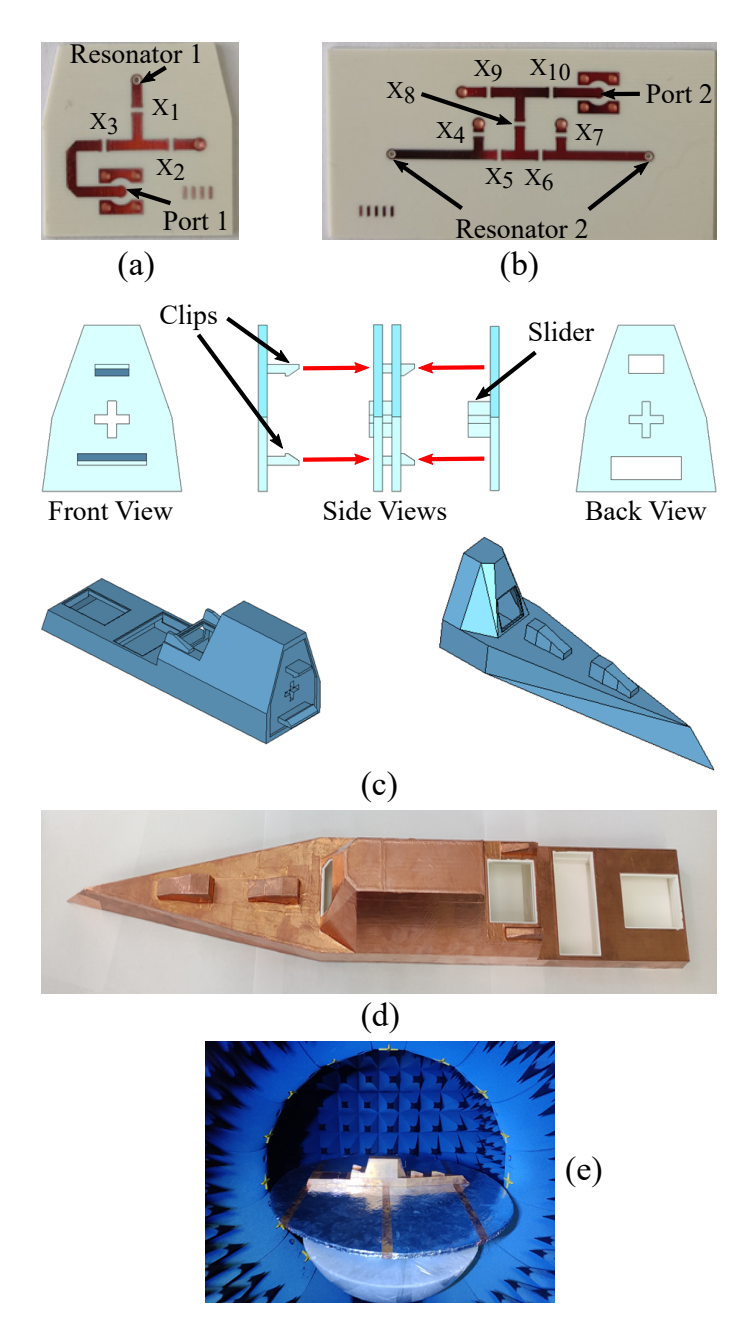


Figure 3.8: Photographs of a 1:310 scaled-model fabricated prototype and its feed network. Coaxial connectors are placed beneath the platform and connected to the feed network PCBs inside the hallow 3-D platform. (a)–(b) Layout and photograph of the feed network designed to excite the resonators. (c) 3-D printed platform design with interior cavities used to accommodate the resonators feed networks. Also, design includes a hold mechanics since platform was fabricated in two parts. (d) 3-D printed platform assemble and covered its surfaces with copper tape. (e) Scaled-model completely assemble over a aluminum ground and placed on the anechoic chamber for radiation measurements.

of 0.812 mm. The feed network is implemented on a 0.813 mm thick RO4003C dielectric substrate with dielectric constant of 3.6 and loss tangent of 0.0027. The values of the

lumped-element components used in the fabricated feed networks are provided in Table 3.2. The values of the lumped-element components used in the feed network are slightly different from those used in the simulations. These differences are attributed to the tolerances involved in fabricating the scaled-model prototype as well as slight differences between the simulated and fabricated models (e.g., using copper tape in the fabricated prototype versus solid sheet assumed in the simulated prototype, etc.). Despite these differences, one can easily compensate for these effects by changing the values of the lumped-element components used in the feed network as we have done.

Table 3.2

LUMPED ELEMENT COMPONENT VALUES OF THE MATCHING
NETWORKS OF THE SIMULATED AND FABRICATED SCALED MODEL
AT 620, 1860, AND 3100 MHz.

	Frequency	620	620 MHz		1860 MHz		3100 MHz	
	Type	Sim.	Meas.	Sim.	Meas.	Sim.	Meas.	
	X_1	55 nH	47 nH	2.7 nH	2.2 nH	Short	Short	
Resonator 1	X_2	10 pF	8.2 pF	1.6 pF	1.4 pF	2.0 pF	1.3 pF	
	X_3	Short	Short	Short	Short	0.5 pF	8.2 pF	
	X_4	22 nH	22 nH	1.9 nH	1.9 nH	1.6 nH	1.6 nH	
	X_5	2.7 pF	2.7 pF	1.5 pF	1.5 pF	0.5 pF	$0.5~\mathrm{pF}$	
	X_6	22 nH	22 nH	1.9 nH	1.9 nH	1.6 nH	1.6 nH	
Resonator 2	X_7	2.7 pF	2.7 pF	1.5 pF	1.5 pF	0.5 pF	0.5 pF	
	X_8	115 pF	115 pF	1.5 pF	Short	47 pF	1.5 pF	
	X_9	15 pF	8.2 pF	2.0 pF	2.7 nH	0.8 pF	0.6 pF	
	X_{10}	Short	Short	Short	10 nH	Short	Short	

3.4.3 Measurement Results

The assembled prototype in the anechoic chamber is shown in Fig. 3.8(e). It was put on top of a circular-shaped ground plane with a diameter of 0.82 m, made out of aluminum on top of a cardboard. The S-parameters of the fabricated prototype were measured in the vicinity of 620, 1860, and 3100 MHz (corresponding to 2 MHz, 6 MHz, and 10 MHz for the

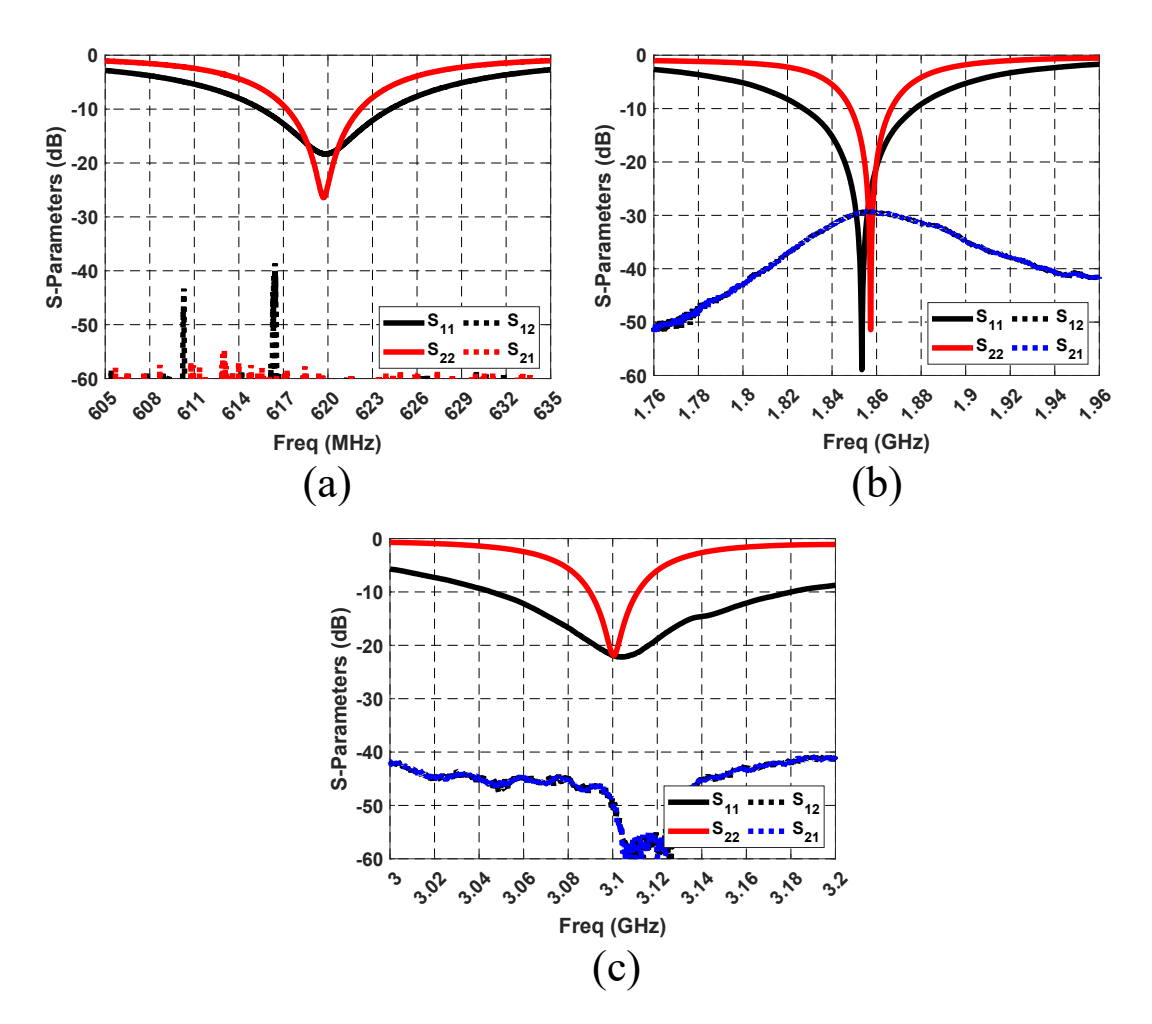


Figure 3.9: Measured S-parameters of the scaled-model of the platform-based NVIS MIMO Channel capacity. Resonators Match to (a) 620 MHz (2 MHz), (b) 1860 MHz (6 MHz), and (c) 3100 MHz (10 MHz).

full-scale model). Fig. 3.9 shows the measured S-parameters in the vicinity of the 620 MHz, 1860 MHz, and 3100 MHz. Observe that the input reflection coefficients are below -10 dB for each antenna and the mutual coupling between the two resonators remains below -30 dB.

The realized gain patterns (both magnitudes and phases) of the fabricated prototypes were measured with a multi-probe near-field system (SATIMO StarLab). The measurements were performed by exciting one antenna at a time (when the other was terminated with 50 Ω). Through this process, complete three dimensional realized gain pattern (magnitudes and phases for both θ and ϕ polarizations) for each resonator was obtained at three frequencies of 620, 1860, and 3100 MHz. The measurement results were post processed in Matlab. Fig.

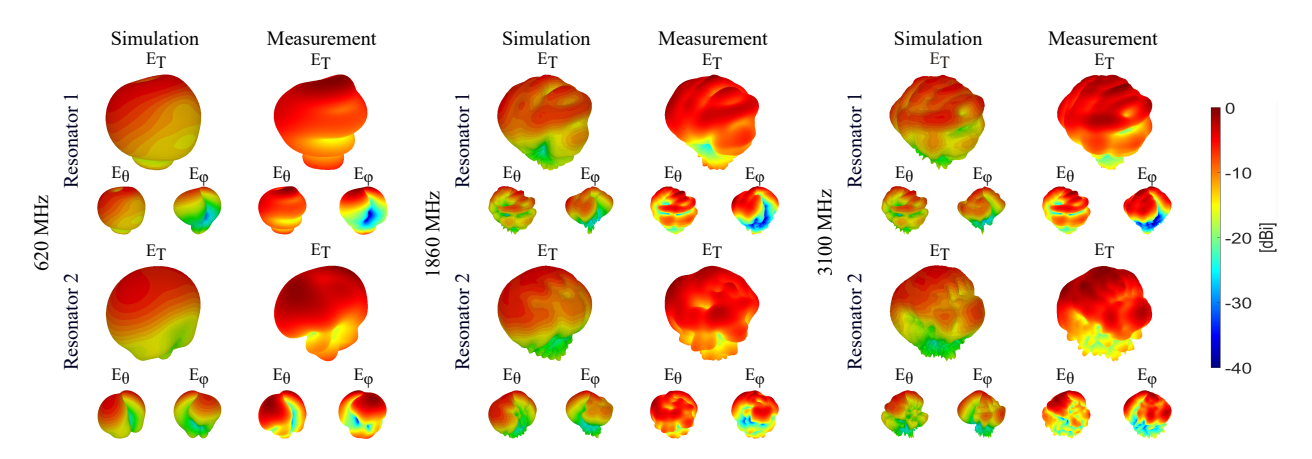


Figure 3.10: Simulated and measured realized gain radiation patterns of the fabricated prototype model at 620, 1860, and 3100 MHz.

3.10 shows the realized gain total, θ , and ϕ at 620, 1860, and 3100 MHz (corresponding to 2, 6, and 10 MHz for the full-scale model) for the simulated and measure radiation patterns. As can be observe in Fig. 3.10 the orthogonality between modes are maintained across the NVIS frequencies. However, at the lower end of the NVIS frequencies, there is significant radiation towards $\theta = 0^{\circ}$, because of the ground dimensions. Also, part of that radiation is attributed to the presence of a large feeding cable connected to the platform, which was not modeled in the simulations.

The total measured and simulated radiation efficiencies of each mode of the scaled-model prototype are reported in Table 3.3. Several factors contribute to reducing the radiation efficiencies of the antennas. The first factor is the small physical dimensions of the antennas (0.03 m), which results large fabrication error when it comes to fabrication process. Second factor is the quality factor of the capacitors at the higher end (3100 MHz), their corresponding quality factor is reduced significantly at higher frequencies lowering the measure efficiencies. The other minor factor such as surface roughness and finite conductivity of the copper tapes and aluminum sheets used in the fabrication of the prototype and the ground plane are potential contributing factors too. Fig. 3.11 shows the channel capacity of the 2×2 using the designed resonators with two orthogonal dipoles above earth at shore. The capacity has been reduced since the efficiency is been reduced at higher frequencies. The channel capacity

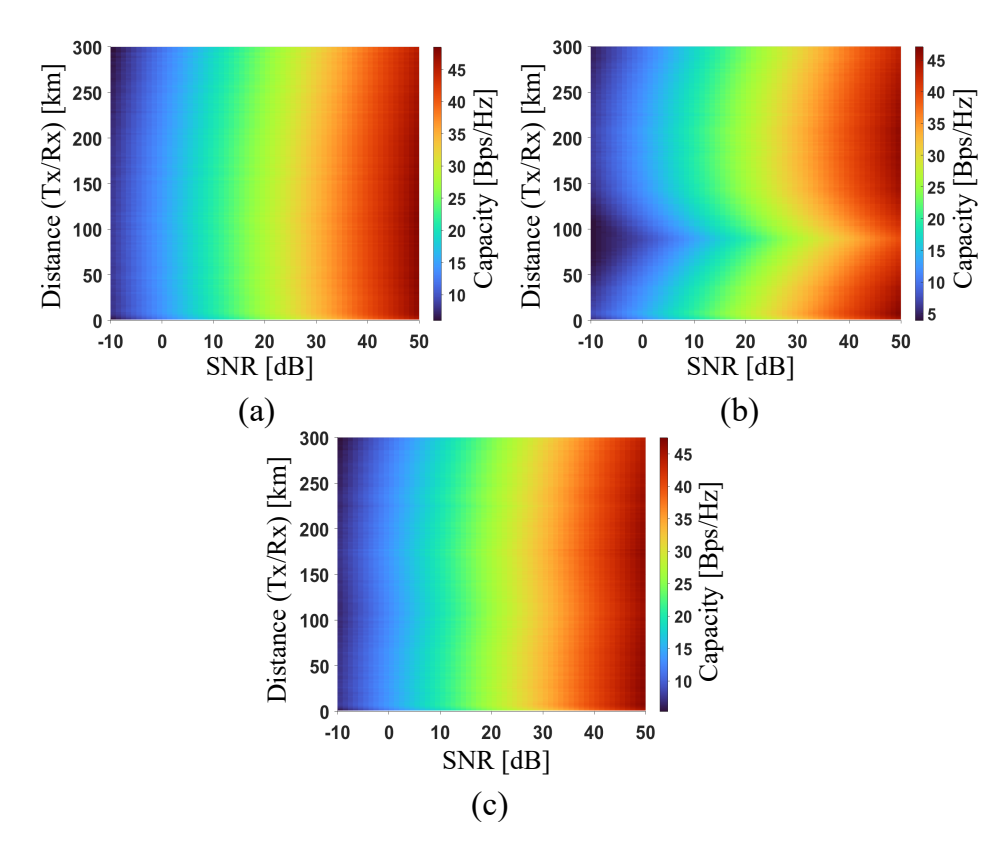


Figure 3.11: NVIS MIMO channel capacity using the two platform resonators with orthogonal dipoles above dry earth at shore. (a) 620 MHz, (b) 1860 MHz, and (c) 3100 MHz (corresponding to 2, 6, and 10 MHz for the full-scaled model).

Table 3.3
SIMULATED AND MEASURED TOTAL
EFFICIENCIES OF THE COUPLING ELEMENTS
USED TO EXCITE DIFFERENT MODES.

Frequency	Reson	ator 1 [dB]	Resonator 2 [dB]		
Trequency	Sim.	Meas.	Sim.	Meas.	
620 MHz	-10.3	-10.8	-16.0	-16.9	
$1860~\mathrm{MHz}$	-0.3	-1.9	-6.3	-7.6	
$3100~\mathrm{MHz}$	-0.3	-0.7	-4.8	-6.7	

of the measurement results required using the radiation patterns and efficiencies in the HF band since the channel capacity algorithm was design for that band. The results are compare with simulation for a more precise characterization on the Appendix C.

3.5 Conclusion

We reported the design and experimental characterization of a ship-to-shore MIMO, platform-based system capable of maximizing NVIS channel capacity. The proposed design is based on exciting two two multi-CMs exploiting the polazitation diversity for HF MIMO system. One mode excites multiple CMs with radiation patterns along the platform and the other excited CMs with radiation patterns across the platform. By properly combining the resonators of the platform with two horizontal dipole above ground at shore we can maximize the channel capacity for NVIS communication. The suitable resonators along with their associated feed and impedance matching networks were designed to excite each of these CMs. Full-wave electromagnetic simulations of the full-scale model of the proposed system were performed and demonstrated that the system can generate and maintain the radiation patterns across the frequency range of 2–10 MHz within the HF band.

To experimentally verify the operation of the proposed antenna, a 1:310 scaled-model prototype along with the required baluns and matching networks were fabricated and experimentally characterized. Both S-parameter and radiation pattern measurements were performed in the vicinity of 620, 1860, and 3100 MHz (corresponding approximately to 2, 6, and 10 MHz for the full-scale model). Note that the losses of the full-scaled model are lower than those of the scaled-model prototype because the lumped elements used in the impedance matching network have significantly lower losses at the HF band. Measurement results demonstrated that good impedance matching can be achieved and the mutual coupling between the different resonators is small (below -30 dB). Furthermore, it was demonstrated the radiation patterns of the two different resonators maintain their polarization across the entire frequency band of interest. The overall antenna efficiency is adversely impacted by the antenna size as well as the losses of the balun and the matching networks used to feed the antenna. Even small losses of the matching network can be amplified significantly due to the larger difference between the input and output VSWRs of the matching network (i.e.,

matched loss magnification [69]). This factor in conjunction with the small quality factor of the capacitors at higher frequencies are the two primary factors contributing to the relatively low measured radiation efficiencies.

Chapter 4

Future Work

4.1 Experimental Demonstration of a Primary-Secondary Synchronization for Distributed Transmit Beamforming Antenna Array

Distributed transmit beamforming systems have been mainly studied due to their potential to improve communication reliability. However, distributed transmit beamforming systems operating in the HF band can be implemented for military applications such as jamming, long-range, and direction finding. The distributed networks of multiple transmitters cooperate to transmit a coherently directional radiation pattern. This improves the performance of transmission resulting in a high-power radiation. The distributed transmit system acts as an antenna array with the capability of steering the beam and focusing energy toward a desired direction. Due to the large wavelengths in the HF band, most military antennas are implemented on moving platforms with space constraints.

The goal of this research will be to experimentally demonstrate a distributed transmit beamforming using a time synchronization algorithm to reduce the phase error between transmitting nodes. This will be accomplished by using a primary-secondary algorithm on a time-slot configuration. The time-slot will allow the time synchronization between radios using a GPS module as external oscillator. Our preliminary results are outlined as follows.

4.1.1 Node Configuration for Experimental Demonstration

To experimentally demonstrate the distributed transmit beamforming, we first need to look into commercially available open-source software-defined radios (SDR). The synchronization method has to be use in multiple nodes, each of which represent a single radio. Each radio needs to be able to use an external oscillator to obtain a more precise synchronization between nodes. The best option is the HackRF One from Great Scott Gadges with the clock input of 10 MHz and the operation frequency of 1–6000 MHz [79]. The HackRF One is an

open-hardware platform capable to be used as an USB peripheral and implement a software radio algorithm in GNURadio [80]. Fig. 4.1 shows the transceiver HackRF One hardware and the board circuitry. The HackRF One can be ordered with an ANT 500 and they work perfectly together. Note, the HackRF One is capable of one pulse-per-second (PPS) external oscillator for algorithms that required better time synchronization [81]. However, implementing one PPS external oscillator would require access to the HackRF circuitry. Furthermore, the external oscillator for the synchronization we selected was a GPS module with the advantages of being high precision, and programmable, and having one PPS output with a UTC time synchronization. The specific GPS module selected for the demonstration was the I-Lotus M12M Timing Oncore [82].



Figure 4.1: HackRF One from Great Scott Gadget. Figure available from [79].

4.1.2 Experimental Architecture on Distributed Transmit Beamforming

A distributed system design is ideal for a platform-based, electrically-small antenna operating in the HF band. In fact, the distribution can effectively increase the efficiency toward a desired target. We use the simplest distributed system with a primary-secondary architecture consisting of a single primary and a single secondary to test our distributed beamforming. In addition, we use time-slotted schedule to accommodate steps for synchronization and transmit beamforming message. Although this method can be implemented using several nodes, we would use only two transmitters and a single receiver, for the proof of concept, to measure the radiation pattern. Fig. 4.2 shows the timeslot diagram to establish synchronization, and

beamforming it also shows the system model for the nodes transmitting toward a target. We are planning to implement the distributed transmit beamforming at the target carrier frequency of 50 MHz.

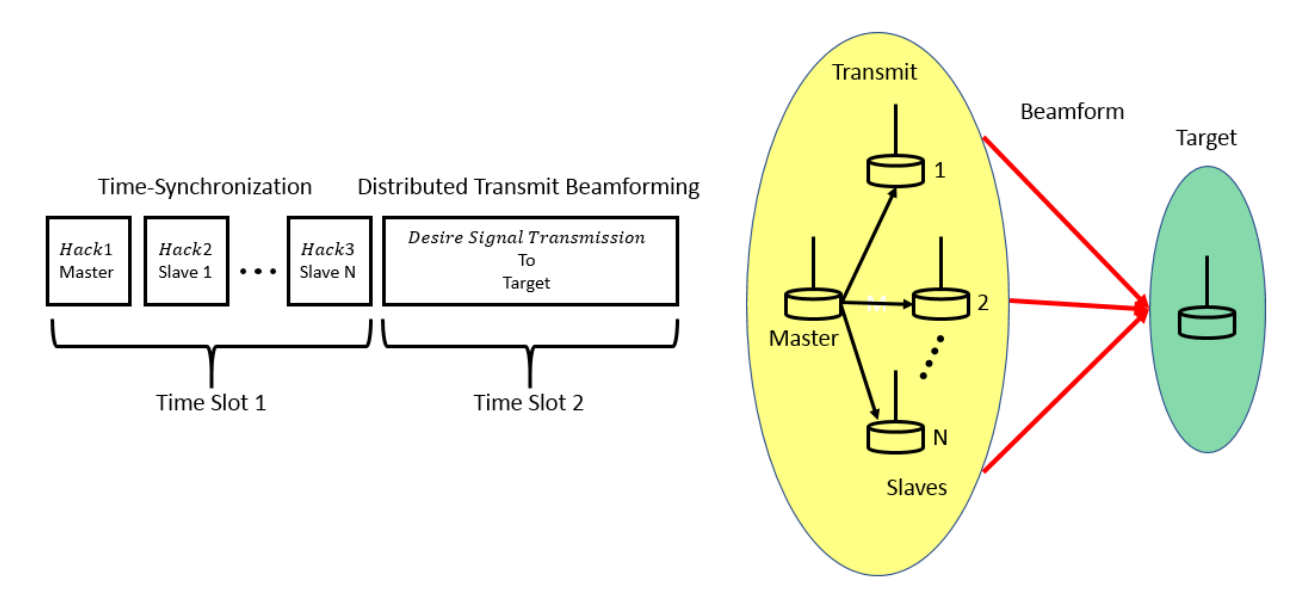


Figure 4.2: Disitributed transmit beamforming concentrating the beam direction toward a desired target without any feedback from the target.

4.1.3 Time-Slotted Synchronization Using GNURadio

In order to optimize the design of the time-synchronization architecture, it is necessary to develop accurate intercommunication between the primary transceiver and the secondary. Moreover, the algorithm will be implemented on the open-source software GNU Radio. On the time-slot for synchronization, the secondary would require demodulation of the received signal of the primary containing the carrier phase for time synchronization. It should be noted that this signal would contain the location data. Since the receiver would also use an external oscillator, we would calculate the phase difference of the carrier frequency before radiating toward the desired target. Furthermore, the localization of the primary is for the offset phase required for the beamform toward the desire direction. Fig. 4.3 shows a simple schematic of the GNU Radio capable of doing synchronization, with the local oscillator of the HackRF instead of using the external GPS module for local carrier synchronization

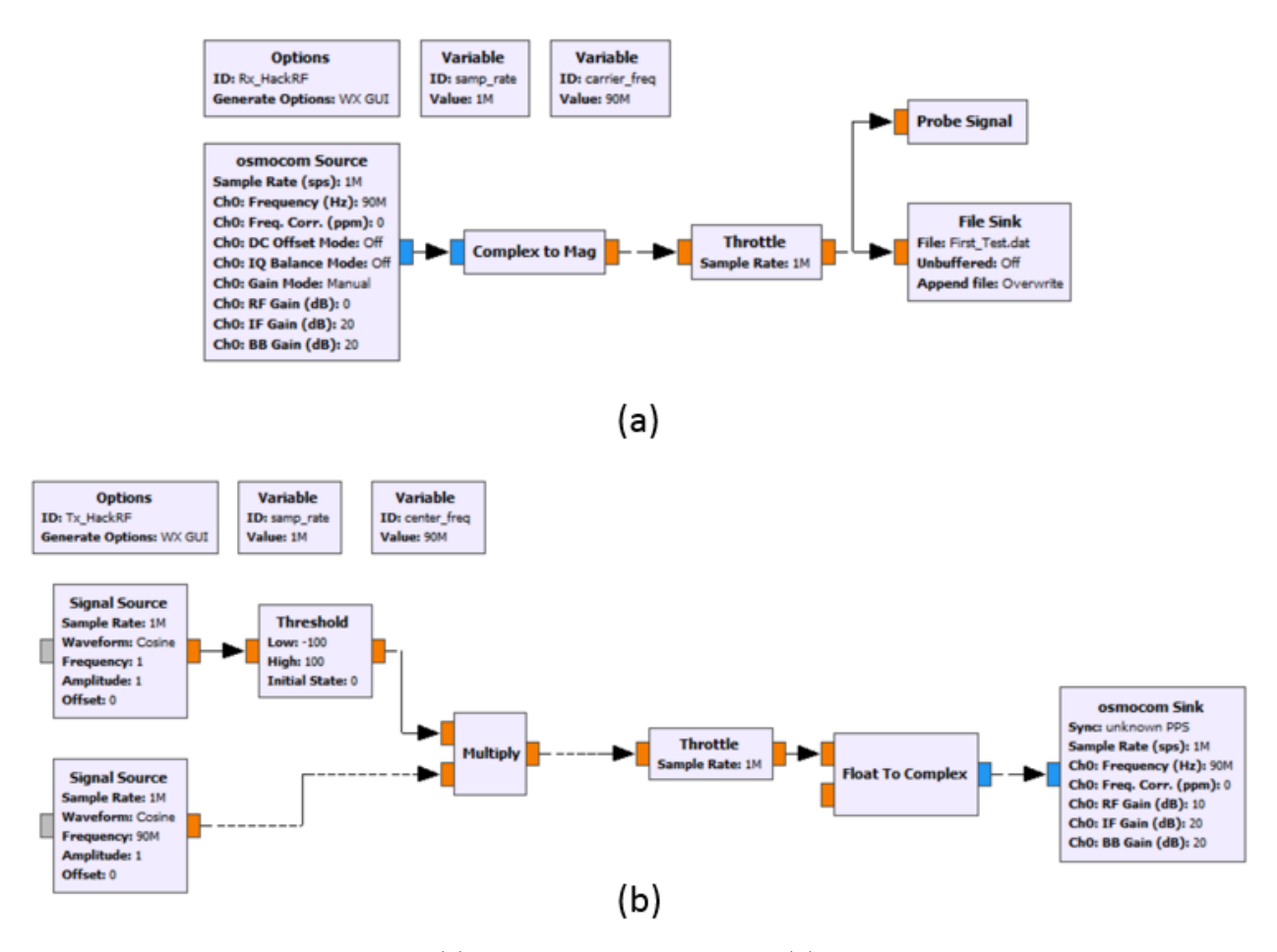


Figure 4.3: GNU Radio software (a) receiver node schematic, (b) transmitting node schematic. This schematic used the local oscillator of the HackRF One

References

- [1] X. Lin, S. Bao, G. Wei, and X. Piao, "The application of directional antenna in stratospheric communication," in *Proc. IET Int. Conf. Commun. Technol.* Appl. (ICCTA), Beijing, China, 2011, pp. 85-88, Oct. 14-16.
- [2] S. W. Ellingson et al., "The long wavelength array," Proc. IEEE, vol. 97, no. 8, pp. 1421-1430, Aug. 2009, doi: 10.1109/JPROC.2009.2015683.
- [3] J. Shin and D. H. Schaubert, "A parameter study of stripline-fed Vivaldi notchantenna arrays," *IEEE Trans. Antennas Propag.*, vol. 47, no. 5, pp. 879-886, May 1999.
- [4] R. Schlub, J. Lu, and T. Ohira, "Seven-element ground skirt monopole ESPAR antenna design from a genetic algorithm and the finite element method," *IEEE Trans. Antennas Propag.*, vol. 51, no. 11, pp. 3033-3039, Nov. 2003.
- [5] P. J. Baldwin, A. G. P. Boswell, D. C. Brewster, and J. S. Allwright, "Iterative calculation of ship-borne HF antenna performance," Proc. Inst. Elect. Eng. H Microw. Antennas Propag., vol. 138, no. 2, pp. 151-158, Apr. 1991.
- [6] S. A. Sanghai, M. Ignatenko, and D. S. Filipovic, "Low-profile two-arm inverted-L antenna design for vehicular HF communications," *IEEE Trans. Antennas Propag.*, vol. 65, no. 11, pp. 5710-5719, Nov. 2017.
- [7] G. Marrocco, L. Mattioni, and V. Martorelli, "Naval structural antenna systems for broadband HF communications—part II: design methodology for real naval platforms," *IEEE Trans. Antennas Propag.*, vol. 54, no. 11, pp. 3330-3337, Nov. 2006.

- [8] C. Wang, Y. Chen, and S. Yang, "HF band aircraft integrated multi-antenna system designs using characteristic modes," in *Proc. 11th Eur. Conf. Antennas Propag. (EUCAP)*, Paris, France, Mar. 19-24, 2017, pp. 1772-1776.
- [9] L. J. Chu, "Physical limitations of omni-directional antennas," J. Appl. Phys., vol. 19, no. 12, pp. 1163-1175, Dec. 1948.
- [10] H. A. Wheeler, "Fundamental limitations of small antennas," Proc. IRE, vol. 35, no. 12, pp. 1479-1484, Dec. 1947.
- [11] R. C. Hansen, "Fundamental limitations in antennas," *Proc. IEEE*, vol. 69, no. 2, pp. 170-182, Feb. 1981.
- [12] T. Shih and N. Behdad, "Bandwidth enhancement of platform-mounted HF antennas using the characteristic mode theory," *IEEE Trans. Antennas Propag.*, vol. 64, no. 7, pp. 2648-2659, July 2016.
- [13] R. Ma, T. Shih, and N. Behdad, "Design of bandwidth-enhanced platform-mounted electrically small VHF antennas using the characteristic-mode theory," IEEE Antennas Wireless Propag. Lett., vol. 17, no. 12, pp. 2384-2388, Dec. 2018.
- [14] F. A. Dicandia, S. Genovesi, and A. Monorchio, "Null-steering antenna design using phase-shifted characteristic modes," *IEEE Trans. Antennas Propag.*, vol. 64, no. 7, pp. 2698-2706, Jul. 2016.
- [15] S. Sow, L. Guo, S. Zhou, and T. Chio, "Electrically small structural antenna design for small UAV based on characteristics modes," in *Proc. 11th Eur. Conf.* Antennas Propag. (EUCAP), Paris, France, Mar. 2017, pp. 2134-2138.
- [16] R. Ma and N. Behdad, "Design of Platform-based HF direction-finding antennas using the characteristic mode theory," *IEEE Trans. Antennas Propag.*, vol. 67, no. 3, pp. 1417-1427, Mar. 2019.

- [17] Y. Chen and C. Wang, "HF band shipboard antenna design using characteristic modes," *IEEE Trans. Antennas Propag.*, vol. 63, no. 3, pp. 1004-1013, 2015.
- [18] S. Mosleh, J. Abouei, and M. R. Aghabozorgi, "Distributed opportunistic interference alignment using threshold-based beamforming in MIMO overlay cognitive radio," *IEEE Trans. Veh. Technol.*, vol. 63, no. 8, pp. 3783-3793, Oct. 2014.
- [19] T. Kaiser, A. Wilzeck, M. Berentsen, and M. Rupp, "Prototyping for MIMO systems an overview," in 2004 12th European Signal Processing Conference, Vienna, 2004, pp. 681-688.
- [20] O. Hiari and R. Mesleh, "A reconfigurable SDR transmitter platform architecture for space modulation MIMO techniques," *IEEE Access*, vol. 5, pp. 24214-24228, 2017.
- [21] S. D. Gunashekar et al., "The use of heterogeneous antenna arrays in experimental HF-MIMO links," in 2009 3rd European Conference on Antennas and Propagation, Berlin, 2009, pp. 1415-1418.
- [22] S. M. Feeney et al., "Compact antenna arrays for HF MIMO applications," in The Institution of Engineering and Technology 11th International Conference on Ionospheric radio Systems and Techniques (IRST 2009), Edinburgh, 2009, pp. 1-5.
- [23] S. M. Feeney, S. Salous, E. M. Warrington, and S. D. Gunashekar, "HF MIMO measurements using spatial and compact antenna arrays," in 2011 XXXth URSI General Assembly and Scientific Symposium, Istanbul, 2011, pp. 1-4.

- [24] H. Krim and M. Viberg, "Two decades of array signal processing research: the parametric approach," *IEEE Signal Process. Mag.*, vol. 13, no. 4, pp. 67-94, Jul. 1996.
- [25] A. Afana, A. Ghrayeb, V. R. Asghari, and S. Affes, "Distributed beamforming for two-way DF relay cognitive networks under primary–secondary mutual interference," *IEEE Trans. Veh. Technol.*, vol. 64, no. 9, pp. 3918-3930, Sept. 2015.
- [26] J. P. Rode, K. Gregorian, J. Ward, and A. Husain, "Collaborative beamfocusing radios (COBRA): A reciprocity based distributed beamforming system," in RWS, Austin, TX, 2016, pp. 51-53.
- [27] S. Amini, D. Na, and K. Choi, "Performance comparison between distributed beamforming and clustered beamforming," in *ITNG*, Las Vegas, NV, 2014, pp. 174-179.
- [28] R. Mudumbai, G. Barriac, and U. Madhow, "On the feasibility of distributed beamforming in wireless networks," *IEEE Trans. Wireless Commun.*, vol. 6, no. 5, pp. 1754-1763, May 2007.
- [29] R. Mudumbai, B. Wild, U. Madhow, and K. Ramchandran, "Distributed beamforming using 1 bit feedback: from concept to realization", in *Proc. 44th Aller-ton Conf. Commun. Control Comput.*, Monticello, IL, Sept. 27-29 2006.
- [30] R. Garbacz, "Modal expansions for resonance scattering phenomena," Proc. IEEE, vol. 53, no. 8, pp. 856–864, Aug. 1965.
- [31] R. Garbacz and R. Turpin, "A generalized expansion for radiated and scattered fields," *IEEE Trans. Antennas Propag.*, vol. AP-19, no. 3, pp. 348-358, May 1971.

- [32] R. Harrington and J. Mautz, "Theory of characteristic modes for conducting bodies," *IEEE Trans. Antennas Propag.*, vol. 19, no. 5, pp. 622-628, Sep. 1971.
- [33] R. F. Harrington and J. Mautz, "Computation of characteristic modes for conducting bodies," *IEEE Trans. Antennas Propag.*, vol. AP-19, no. 5, pp. 629–639, Sep. 1971.
- [34] M. Cabedo-Fabres, E. Antonino-Daviu, A. Valero-Nogueira, and M. Bataller, "The theory of characteristic modes revisited: A contribution to the design of antennas for modern applications," *IEEE Antennas Propag. Mag.*, vol. 49, no. 5, pp. 52–68, Oct. 2007.
- [35] E. Antonino-Daviu, M. Cabedo-Fabres, M. Ferrando-Bataller, and J. I. Herranz-Herruzo, "Analysis of the coupled chassis-antenna modes in mobile handsets," in *IEEE Antennas Propag. Soc. Symposium*, 2004., Monterey, CA, USA, 2004, pp. 2751-2754 Vol.3.
- [36] J. Villanen, J. Ollikainen, O. Kivekas, and P. Vainikainen, "Compact antenna structures for mobile handsets," in *IEEE 58th Veh. Technol. Conf. VTC*, Orlando, FL, 2003, pp. 40-44 Vol.1.
- [37] H. Li and B. K. Lau, "Design of low profile MIMO antennas for mobile handset using characteristic mode theory," in *IEEE 5th Asia-Pacific Conf. Antennas Propag. (APCAP)*, Kaohsiung, 2016, pp. 63-64.
- [38] R. Mittra and A. Kumar, "Study of antenna systems located on complex platforms by using characteristic mode analysis and related techniques," in *IEEE Int. Symp. Antennas Propag. & USNC/URSI Nat. Rad. Sci. Meeting*, San Diego, CA, USA, Jul. 9-14, 2017, pp. 1159-1160.

- [39] R. Mittra and A. Kumar, "Antenna placement on complex platforms by using characteristic mode analysis and characteristic basis function technique," in Proc. Int. Symp. Antennas Propag. (ISAP), Phuket, Oct. 30-Nov. 2, 2017, pp. 1-2.
- [40] R. Martens, E. Safin, and D. Manteuffel, "Inductive and capacitive excitation of the characteristic modes of small terminals," in *Proc. Loughborough Antennas Propag. Conf. (LAPC)*, Loughborough University, UK, Nov. 14-15, 2011, pp. 1-4.
- [41] B. A. Witvliet and R. M. Alsima-Pagès, "Radio communication via near vertical incidence skywave propagation: an overview," *Telecommun. Syst.* 66, 295-309 (2017), doi: 10.1007/s11235-017-0287-2.
- [42] B. A. Witvliet et al., "Measuring the isolation of the circularly polarized characteristic waves in NVIS propagation [measurements corner]," *IEEE Ant. Prop. Mag.*, vol. 57, no. 3, pp. 120-145, June 2015, doi: 10.1109/MAP.2015.2445633.
- [43] J. Chalas, K. Sertel, and J. L. Volakis, "NVIS synthesis for electrically small aircraft using characteristic modes," in 2014 IEEE Ant. Propag. Soc. Int. Symp. (APSURSI), 2014, pp. 1431-1432, doi: 10.1109/APS.2014.6905041.
- [44] K. Davies, "Oblique propagation," *Ionopheric Radio Propagation*, Eds. Virginia, VA, USA: Univ. of Virginia, 1966, pp. 159–214.
- [45] S. Enserink, C. Köse, M. Fitz, M. Urie, and R. McCourt, "A model for dual polarized HF MIMO communications," *IEEE Military Comm. Conf.*, 2015, pp. 1650-1655, doi: 10.1109/MILCOM.2015.7357681.

- [46] A. Västberg and B. Lundborg, "Superposition of signals in ionospheric multipath channels," *Radio Science*, vol. 32, no. 5, pp. 2083-2090, Sept.-Oct. 1997, doi: 10.1029/97RS00320.
- [47] Method for the prediction of the performance of HF circuits, Rec. ITU-R P.533-14, International Telecommunication Union, Geneva, Switzerland, Aug. 2019.
- [48] C. Watterson, J. Juroshek, and W. Bensema, "Experimental confirmation of an HF channel model," inc *IEEE Trans. Comm. Tech.*, vol. 18, no. 6, pp. 792-803, December 1970, doi: 10.1109/TCOM.1970.1090438.
- [49] S. Aust, R. V. Prasad, and I. G. M. M. Niemegeers, "Performance study of MIMO-OFDM platform in narrow-band sub-1 GHz wireless LANs," in 2013 11th International Symposium and Workshops on Modeling and Optimization in Mobile, Ad Hoc and Wireless Networks (WiOpt), Tsukuba Science City, 2013, pp. 89-94.
- [50] X. Zhao, S. P. Yeo, and L. C. Ong, "Planar UWB MIMO antenna with pattern diversity and isolation improvement for mobile platform based on the theory of characteristic modes," *IEEE Trans Antennas Propag.*, vol. 66, no. 1, pp. 420-425, Jan. 2018.
- [51] L. Y. Nie, X. Q. Lin, Z. Q. Yang, J. Zhang, and B. Wang, "Structure-shared planar UWB MIMO antenna with high isolation for mobile platform," *IEEE Trans. Antennas Propag.*, vol. 67, no. 4, pp. 2735-2738, April 2019.
- [52] S. B. Sahay, K. C. Bhagwat, and P. R. J. Mohan, "Exploitation of MIMO techniques for reliable HF communication," in 2012 International Conference on Signal Processing and Communications (SPCOM), Bangalore, 2012, pp. 1-4.

- [53] S. D. Gunashekar et al., "An experimental investigation into the feasibility of MIMO techniques within the HF band," in *The Second European Conference* on Antennas and Propagation, (EuCAP), Edinburgh, 2007, pp. 1-5.
- [54] B. Peiffer, R. Mudumbai, A. Kruger, A. Kumar, and S. Dasgupta, "Experimental demonstration of a distributed antenna array pre-synchronized for retrodirective transmission," in CISS, Princeton, NJ, 2016, pp. 460-465.
- [55] J. Diao, M. Hedayati, and Y. E. Wang, "Experimental demonstration of distributed beamforming on two flying mini-drones," in *USNC-URSI NRSM*, Boulder, CO, USA, 2019, pp. 1-2.
- [56] J. Proakis and M. Salehi, "Digital Cellular Communications Systems," in Communication Systems Engineering, 2 ed., Pearson, 2001, ch. 10, sec. 4.2, pp. 766-774.
- [57] P. Bidigare et al., "Implementation and demonstration of receiver-coordinated distributed transmit beamforming across an ad-hoc radio network," in ASILO-MAR, Pacific Grove, CA, 2012, pp. 222-226.
- [58] H. Ouassal, T. Rocco, M. Yan, and J. A. Nanzer, "Decentralized frequency synchronization in distributed antenna arrays with quantized frequency states and directed communications," *IEEE Trans. Antennas Propag.*, vol. 68, no. 7, pp. 5280-5288, Jul. 2020.
- [59] D. R. Brown III and H. V. Poor, "Time-slotted round-trip carrier synchronization for distributed beamforming," *IEEE Trans. Signal Process.*, vol. 56, no. 11, pp. 5630-5643, Nov. 2008.

- [60] M. Tang, Z. Wu, T. Shi, and R. W. Ziolkowski, "Dual-Band, Linearly Polarized, Electrically Small Huygens Dipole Antennas," *IEEE Trans. Antennas Propag.*, vol. 67, no. 1, pp. 37-47, Jan. 2019.
- [61] W. Lin and R. W. Ziolkowski, "Electrically Small Huygens Antenna-Based Fully-Integrated Wireless Power Transfer and Communication System," *IEEE Access*, vol. 7, pp. 39762-39769, 2019.
- [62] Amphibious Assault Vehicle, Wikipedia, Access: Aug. 2017, [Online]. Available: https://en.wikipedia.org/wiki/Assault_Amphibious_Vehicle.
- [63] Altair FEKO (2017), Altair Hyperworks, Accessed: Sept. 1, 2017. [Online]. Available: https://altairhyperworks.com/product/FEKO/.
- [64] T. Lan, K. Kawabata, and H. Arai, "Utilization of Inverted-F Antenna Elements to Design a Platform-Mounted HF Antenna," in *Int. Conf. Adv. Technol. Commun. (ATC)*, Hanoi, Vietnam, pp. 15-18, 2019, pp. 15-18.
- [65] Karaboikis, Soras, Tsachtsiris, and Makios, "Compact dual-printed inverted-F antenna diversity systems for portable wireless devices," *IEEE Antennas Wireless Propag. Lett.*, vol. 3, pp. 9-14, 2004.
- [66] CST Studio Suite (2018), Dassaults Systemes, Accessed: Sept. 1, 2017. [Online].

 Available: https://www.cst.com/.
- [67] ADS (2016), Keysight Techonologies, Accessed: Sept. 1, 2017. [Online]. Available: https://www.keysight.com/.
- [68] MatLab (2019), MathWorks, Accessed: April 1, 2019. [Online]. Available: https://www.mathworks.com/products/matlab.html.
- [69] R. C. Hansen and R. E. Collin, "Bandwidth and matching," in *Small Antenna Handbook*, ed. Hoboken, NJ, USA: Wiley, 2011, ch. 2, sec. 2.4, pp. 46-48.

- [70] Y. Erhel, D. Lemur, M. Oger, J. Le Masson, and F. Marie, "Evaluation of ionospheric HF MIMO channels: Two complementary circular polarizations reduce correlation," in *IEEE Ant. Propag. Mag.*, vol. 58, no. 6, pp. 38-48, Dec. 2016, doi: 10.1109/MAP.2016.2609799.
- [71] P. R. King and S. Stavrou, "Capacity Improvement for a Land Mobile Single Satellite MIMO System," *IEEE Ant. Wireless Propag. Lett.*, vol. 5, pp. 98-100, 2006, doi: 10.1109/LAWP.2006.872439.
- [72] M. Lupupa and M. E. Dlodlo, "Performance of MIMO system in Weibull fading channel - channel capacity analysis," *IEEE EUROCON*, 2009, pp. 1735-1740, doi: 10.1109/EURCON.2009.5167878.
- [73] U. Umaisaroh, G. Hendrantoro, A. Mauludiyanto, and T. Fukusako, "Capacity of 2×2 MIMO HF NVIS channels with linearly polarized horizontal antennas," in *IEEE Wireless Comm. Lett.*, vol. 8, no. 4, pp. 1120-1123, Aug. 2019, doi: 10.1109/LWC.2019.2908648.
- [74] G. Marrocco, L. Mattioni, and V. Martorelli, "Naval structural antenna systems for broadband HF communications—part II: design methodology for real naval platforms," *IEEE Trans. Antennas Propag.*, vol. 54, no. 11, pp. 3330-3337, Nov. 2006, doi: 10.1109/TAP.2006.884306.
- [75] Testing of HF modems with bandwidths of up to about 12 kHz using ionospheric channel simulators, Rec. ITU-R F.1487, International Telecommunication Union, Geneva, Switzerland, May 2000.
- [76] D. Tse and P. Viswanath, "MIMO I: spatial multiplexing and channel modeling," in *Fundamentals of Wireless Communication*, Eds., Cambridge, MA, USA: Cambridge UP, 2005, pp. 291–309.

- [77] I. E. Telatar, "Capacity of multi-antenna gaussian channels," Euro. Trans. Telecommun., Vol. 10, No. 6, Nov. 1999, pp. 585-596, doi:10.1002/ett.4460100604.
- [78] Zumwalt-class destroyer, Wikipedia, Access: Aug. 2022, [Online]. Available: https://en.wikipedia.org/wiki/Zumwalt-class_destroyer.
- [79] HackRF One, great scott gadgets, Access: Jun. 2020, [Online], Available: https://greatscottgadgets.com/hackrf/one/.
- [80] GNU Radio, GNU Radio: The Free and Open Software Radio Ecosystem, Access: Jun. 2020, [Online], Available: https://www.gnuradio.org/.
- [81] M. Bartolucci, J. A. Del Peral-Rosado, R. Estatuet-Castillo, J. A. Garcia-Molina, and M. Crisci and G. E. Corazza, "Synchronisation of low-cost open source SDRs for navigation applications," in NAVITEC, Noordwijk, Dec. 14-16, 2016, pp.1-7.
- [82] M12M Timing Oncore, I-Lotus: Whats Leading You, Acess: Jun. 2020, [Online], Available: http://www.ilotus.com.sg/m12m_timing_oncore/.

Appendix

A Supplementary Material

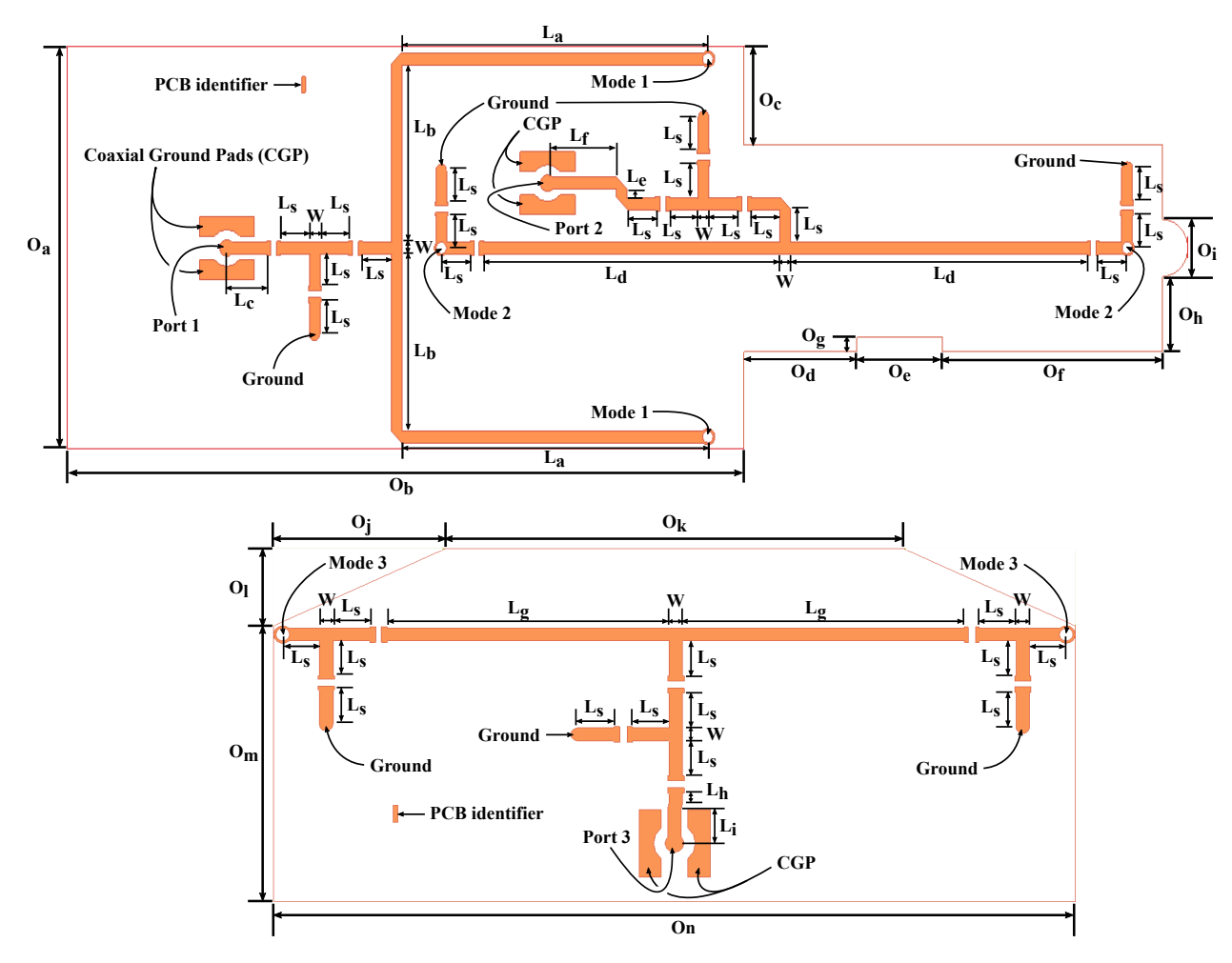


Figure A.1: Detailed layout of the printed circuit boards that include the impedance matching network and the baluns used to feed the antennas on the scaled-model prototype. The top layout includes the feeding and matching network for the coupling elements used to excite Mode 1 and 2 of the platform. The bottom layout includes the feeding and matching network of the coupling element used to excite Mode 3. Table A.1 shows the corresponding values for the variables.

Table A.1						
PHYSICAL DIMENSIONS OF THE FABRICATED FEED NETWORKS WHOSE						
LAYOUTS ARE SHOWN IN FIG. A.1.						

Variable	Length (mm)	Variable	Length (mm)	Variable	Length (mm)
W	1.48	L _h	1.00	$O_{\rm h}$	9.30
L_{s}	4.00	L_{i}	4.00	O_{i}	7.00
$L_{\rm a}$	43.00	O_a	49.71	O_j	18.71
$L_{\rm b}$	21.88	O_{b}	95.00	O_k	50.00
L_{c}	5.57	O_c	12.06	O_1	8.86
$L_{\rm d}$	41.63	O_d	15.86	O_{m}	31.68
$L_{\rm e}$	1.04	O_{e}	12.00	O_n	87.43
$\mathrm{L_{f}}$	9.70	O_{f}	31.00		
L_{g}	30.73	O_g	1.80		

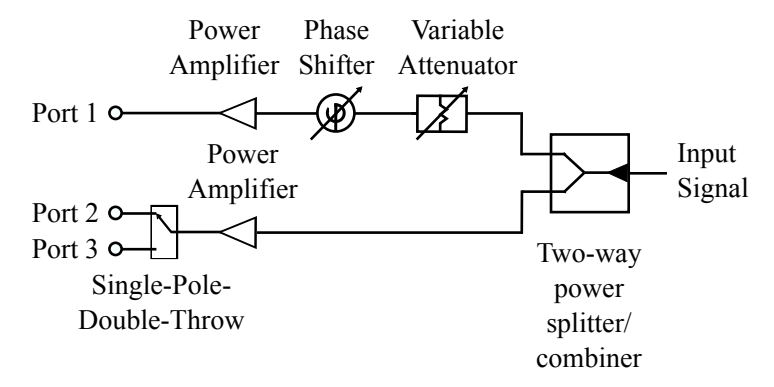


Figure A.2: Topology of one potential active feed network that can be used in the transmit mode in conjunction with the proposed antennas to generate the desired cardioid-shaped radiation patterns. Since the complex excitation coefficient with which the different coupling elements must be excited will change as a function of frequency and as a function of operational environment (e.g., changing different ground types, etc.), using an active feed network is expected to be more efficient. The circuit shown here depicts an active circuit in the transmit mode. A similar circuit can be obtained for the receive mode if the power amplifiers are replaced with low-noise amplifiers. A version of this circuit that can be used for both transmit and receive applications requires using transmit/receive switches to select between the low-noise amplifier in the receive and the power amplifier in the transmit modes.

B Ionosphere Modeling

Fig. B.1 shows the in-house algorithm flowchart con tainting the most important processed for the MIMO NVIS channel capacity calculations. As observer, the upload files are required for specific channel capacity dimension of subset combination of channel capacity dimension using the characteristic modes of a platform as transmitters. However, the flowchart does not discuss the procedure for determine the type of channel capacity or the data provided by the user (each user could used different configuration, subset understudy, frequencies, etc). Important variables has to be determine before hand like coordinates for each of the elements for the transmitters and receiver. Each of the sections (transmitters and receivers) has their own coordinate system and then integrated into a single coordinate system using the separation between transmission and reception. Other important parameters are the distance sweep array, number of repetitions for the stationary ergodic process of the ionosphere model, parameters for the ionosphere model, size for the channel capacity (M \times N), and signal to noise ratio (SNR) sweep levels. The in-house algorithm first calculate all the magnitudes and phases of the transmitters and receivers for each distances separated from the channel capacity to reduce the MatLab time and reconstruct the actual element phase.

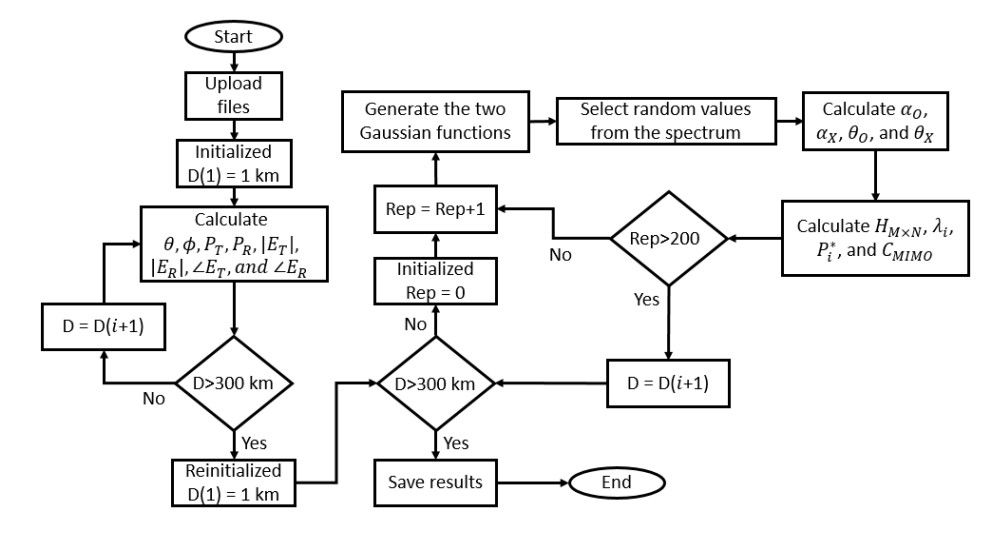


Figure B.1: Basic flowchart of the in-house algorithm used to calculate the NVIS MIMO channel capacity for $M \times N$, but reduced the matrix based on needs.

The tap-gain ionospheric modeling for the NVIS channel capacity in-house algorithm is represented with stationary Gaussian scatter model commonly known as Watterson model. The input wave from the transmitters are attenuated and delay with the ionosphere interaction depending on the type of ionospheric propagation mode or path. However, the modulated signal in amplitude and phase can be approximated with a complex random tap-gain function. Each mode of propagation with the ionosphere can be represented using the following function:

$$G_i(f) = \frac{1}{A_x \sigma_x \sqrt{2\pi}} exp\left[\frac{-(f - f_x)^2}{2\sigma_x^2}\right]$$
 (1)

Fig. B.2(a) present the Gaussian scatter power spectra for a extraordinary/ordinary mode of propagation using the quantitative testing of HF modems for NVIS conditions provided by [75]. The power spectra for each ordinary and extraordinary mode can be created using the same random tap-gain Gaussian function. However, since we need to select two random numbers from the spectra (extraordinary and ordinary modes), we need to limit the spectra to a minimum power levels. Fig. B.2(b) shows the limited spectra to a power level of 0.1. The selected random magnitude value will represent the attenuation of the signal due to the extraordinary and ordinary modes and the frequency shift for that random power level will represent the time delay with respect to the center frequency of cero.

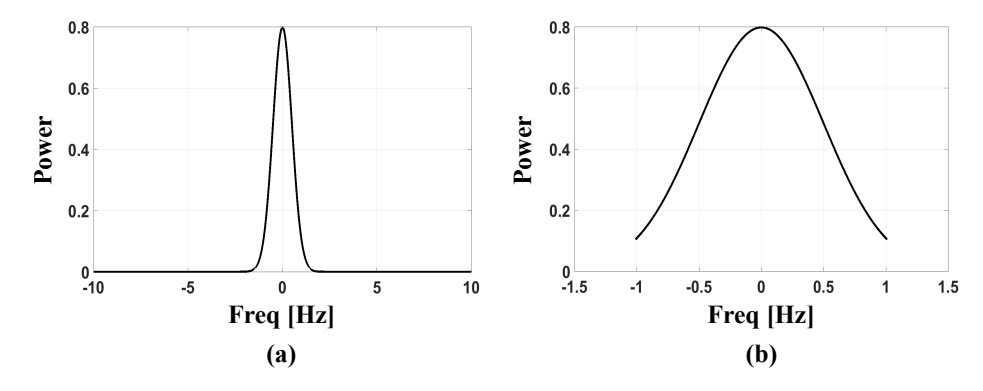


Figure B.2: Tap-gain function represented as a power spectrum of a Gaussian scatter function. Each magneto-ionic component is represented by separated Gaussian scatter functions. (a) Gaussian scatter power spectra.

C Channel Capacity Study

Taking into consideration the NVIS channel capacity in-house algorithm was written for the HF-band, we required to study the channel capacity using the exact frequencies at full size and not the scaled frequencies. Fig. C.1 shows the full size platform channel capacity when the platform is excited with the designed resonators. The channel capacity was calculated with the excited far-field patterns of the platform over sea water as transmitter with the two orthogonal dipoles horizontally placed over dry earth at shore. However, since the platform was scaled for measurements, the results required further comparison. The simulated scaled-model has larger losses due to the ground losses, lumped elements at higher frequencies, and the PCB. Hence, the model far-field patterns and losses were scaled down to their corresponding HF frequencies to study the NVIS channel capacity using the in-house algorithm for comparison with the full size model. Fig. C.2 shows the simulated scaled-model channel capacity using their corresponding HF frequencies. Similarly, the measurement results of the fabricated platform was study. The far-field and efficiency were scaled to the HF frequencies to characterize the NVIS channel capacity using the in-house algorithm for comparison with the simulations. Fig. C.3 shows the measurement scaled-model channel capacity using their corresponding HF frequencies. Consequently, due to the increased losses and far-field patterns differences between simulation and measurement resulting in a channel capacity discrepancy of 8 bps/Hz.

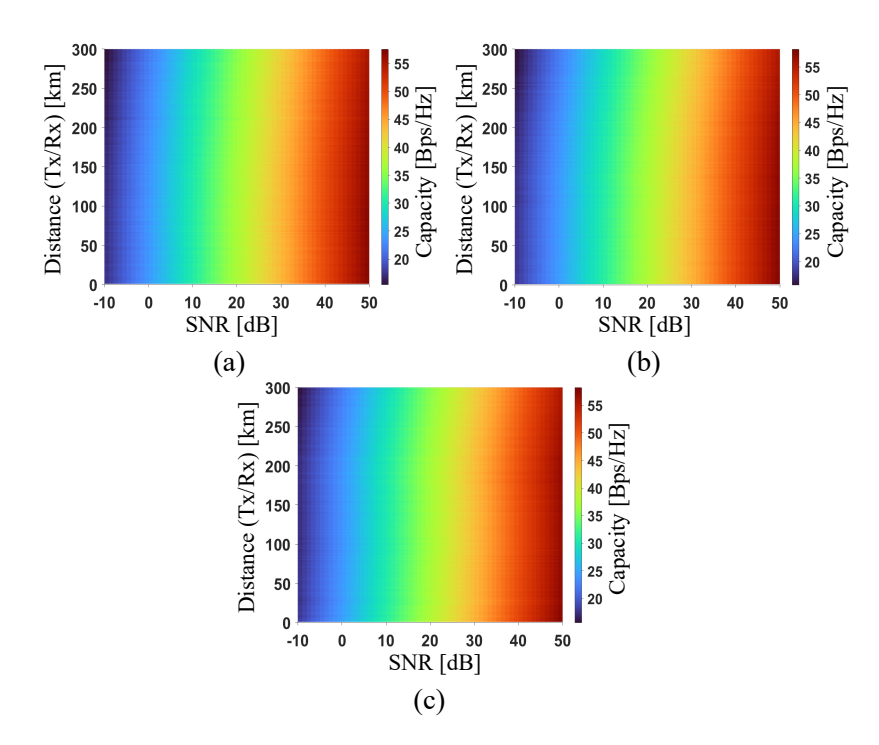


Figure C.1: NVIS MIMO channel capacity of the full size simulated platform with realistic material details excited using the proposed resonators over the platform with the orthogonal dipoles at shore. The channel capacity of the full size 2×2 at (a) 2 MHz, (b) 6 MHz, and (c) 10 MHz.

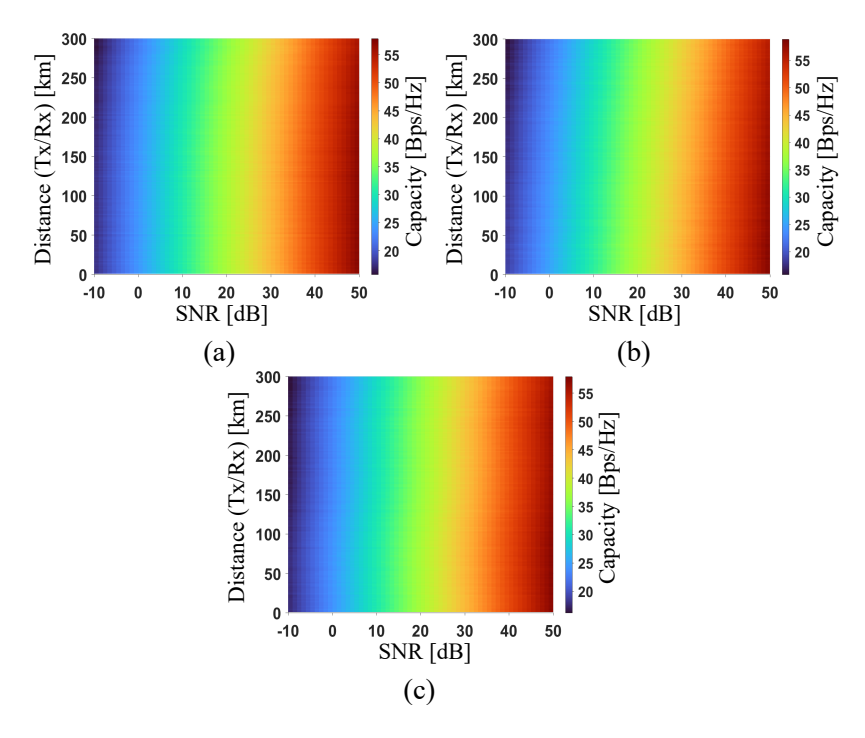


Figure C.2: NVIS MIMO channel capacity of the simulated scaled-model platform with all the realistic details before fabrication (i.e., copper tape, cardboard ground cover with aluminum table, copper resonators, PCB, and lumped-elements). The 2×2 channel capacity of the simulated scaled-model at (a) 620 MHz, (b) 1860 MHz, and (c) 3100 MHz (representing 2 MHz, 6 MHz, and 10 MHz, respectively).

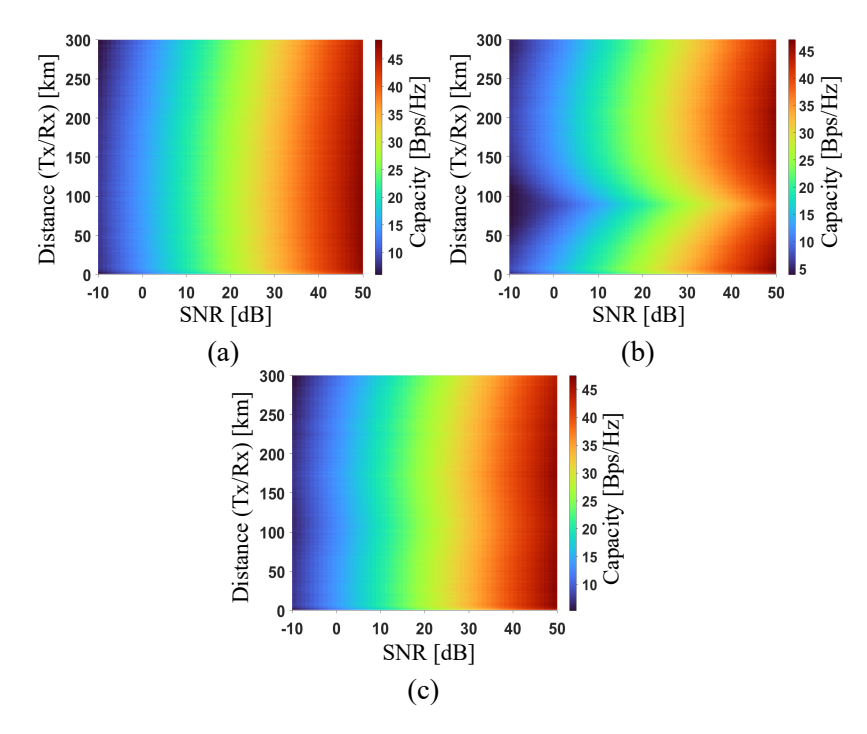


Figure C.3: NVIS MIMO channel capacity of the measured scaled-model platform with all the fabricated details of the proposed resonators over the platform. The 2×2 channel capacity of the scaled-model at at (a) 2 MHz, (b) 6 MHz, and (c) 10 MHz (representing 2 MHz, 6 MHz, and 10 MHz, respectively).